Neuroligin-2 is ubiquitinated by Nedd4l to control developmental astrocyte morphogenesis.

Kristina Sakers[1-2*], Juan J. Ramirez[1,3], Nimrod Elazar[1-2], Leykashree Nagendren[1], Erik Soderblom[1, 3], Cagla Eroglu[1-2,4]

Affiliations:

1. Department of Cell Biology, Duke University Medical Center, Durham, NC, USA
2. Howard Hughes Medical Institute, Duke University Medical Center, Durham, NC, USA
3. Duke Proteomics and Metabolomics Shared Resource and Duke Center for Genomic and Computational Biology, Duke University Medical School, Durham, North Carolina, USA
4. Department of Neurobiology, Duke University Medical Center, Durham, NC, USA

Corresponding Authors:

Kristina Sakers, Ph.D. kristina.sakers@duke.edu

Cagla Eroglu, Ph.D. cagla.eroglu@duke.edu

ABSTRACT

Astrocytes of the central nervous system have an intricate and highly branched morphology. Proper development of perisynaptic astrocyte processes is necessary for the tripartite synapse development, maturation, and function. However, how astrocyte morphogenesis is controlled, and the specific molecules orchestrating this development are largely unknown. Previously, we identified Neuroligins (NLs) 1-3 as regulators of astrocyte morphogenesis by forming transcellular adhesions with neuronal neurexins. Here, we found that NL2 plays a non-redundant essential role in astrocyte morphogenesis. Through structure and function studies, we identified a WW-binding motif within the NL2 intracellular domain required for astrocyte morphogenesis. Using cell-specific *in vivo* proximity labeling by biotinylation (iBioID), we found that each NL displays distinct protein-protein interactions within astrocytes, and NL2 has cell-type specific interactomes in astrocytes versus neurons. By leveraging this interactome, we conducted *in vitro* and *in vivo* candidate screens and identified WW domain-containing E3 ubiquitin ligase Nedd4l to control astrocyte morphogenesis. Biochemical assays revealed that Nedd4l ubiquitinates and stabilizes NL2, and this ubiquitination step is required for astrocyte morphogenesis. This study shows that Neuroligins have non-overlapping roles in controlling astrocyte growth and uncovers a molecular mechanism of how NL2 mediates astrocyte morphogenesis.

INTRODUCTION

Protoplasmic astrocytes of the central nervous system (CNS) are easily identified by their unique bush-like morphology, yet the molecular mechanisms that govern how astrocytes develop and their complex structure are largely unknown. Astrocytes tile the brain and extend fine filopodia-like processes into the neuropil(Bushong et al., 2004, 2002), allowing them to play an active role in critical brain functions including synaptogenesis, regulation of synaptic strength, and buffering of neurotransmitters and ions(Farizatto and Baldwin, 2023; Verkhratsky and Nedergaard, 2018). Human astrocytes are disproportionately larger and more complex than rodent astrocytes(Oberheim et al., 2006), suggesting that higher-order species require astrocytes for advanced-level brain function. Consequently, astrocyte dysfunction has been identified across a myriad of neurological diseases(Tian et al., 2010; Rothstein et al., 1995; Preman et al., 2021; Booth et al., 2017; Gutmann et al., 1999). In particular, a recent study found that numerous Alzheimer's risk genes correlate specifically with astrocyte territory size(Endo et al., 2022). Thus, it is crucial to understand how astrocyte morphogenesis proceeds and which cell biological mechanisms govern this process.

Various signals have emerged as regulators of astrocyte growth, including neuronal-derived secreted factors such as Sonic Hedgehog(Xie et al., 2022) and BDNF(Holt et al., 2019), actin-binding proteins including Ezrin(Endo et al., 2022; Lavialle et al., 2011) and Profilin-1(Molotkov et al., 2013), and numerous cell-adhesion molecules(Baldwin et al., 2023). Amongst the latter, Neuroligins (NLs) play a critical role in the morphogenesis of astrocytes(Ackerman et al., 2021; Stogsdill et al., 2017), as well as oligodendrocyte precursor cells(Li et al., 2024). NLs are trans-synaptic cell-adhesion proteins that bind to

59 Neurexins to promote synaptic formation(Barrow et al., 2009; Chih et al., 2005;
60 Scheiffele et al., 2000; Shipman and Nicoll, 2012), and function(Babaev et al., 2016;
61 Varoqueaux et al., 2006). There are four NL genes expressed in rodents, with NL 1, 2,
62 and 3 being the predominant family members. A limited number of studies have been
63 conducted to investigate how NLs control the outgrowth and complexity of neuronal
64 processes. In rodent neurons, NL1 dose-dependently controls dendritic morphology,
65 wherein NL1 overexpression increases, and NL1 knockdown decreases, dendritic
66 arborization(Schnell et al., 2014, 2012). In contrast, loss of NL3 results in a more
67 complex dendritic arbor(Xu et al., 2019), suggesting non-overlapping roles for NLs in
68 controlling neuronal morphology. Moreover, neuronal NLs were also found to have non-
69 redundant roles in their control of synaptic function(Chanda et al., 2017; Nguyen et al.,
70 2016). In astrocytes, loss of NLs 1-3 each reduces astrocyte territory and neuropil
71 infiltration size(Stogsdill et al., 2017). However, whether NLs play unique roles in
72 astrocyte morphogenesis and what mechanisms control this process is unclear. NLs are
73 implicated in neurodevelopmental diseases including Autism Spectrum Disorder(Jamain
74 et al., 2003; Parente et al., 2017) and thus, it is imperative to understand NL function
75 across all cell types throughout development.

76 Functional differences across NLs may stem from divergence in amino acid sequence.
77 Rodent NLs 1-3 have similar extracellular domains (ECD, ~75% similarity) and more
78 disparate intracellular domains (ICD, ~50% similarity). Within the ICD, several amino
79 acid motifs have been shown to direct interactions with specific protein partners,
80 ultimately leading to unique functional consequences such as the specification of
81 inhibitory versus excitatory synapses(Poulopoulos et al., 2009; Shipman et al., 2011;

82 Sumita et al., 2007). One study using chimeric NLs demonstrated that NL function is not
83 solely dependent on Neurexin binding to the ECD, but also requires interactions with
84 intracellular proteins in the cytosol to control synapse-specific functions(Nguyen et al.,
85 2016). Further, post-translational modifications on NL ICDs can influence protein-protein
86 interactions and downstream signaling. For example, NL1 tyrosine phosphorylation at
87 Y782 results in preferential binding to the excitatory presynaptic marker PSD-95 over
88 the inhibitory postsynaptic scaffold protein Gephyrin. PSD95 then recruits α-amino-3-
89 hydroxy-5-methyl-4-isoxazolepropionic acid (AMPA) receptors and controls synaptic
90 firing(Giannone et al., 2013; Letellier et al., 2018). Yet, previous studies have been
91 conducted in a neuronal context, and thus, whether astrocytic NLs have distinct protein-
92 protein interactions and how these interactions control astrocyte development is still
93 unknown.

94 In this study, we show that NLs 1-3 have non-overlapping roles in controlling astrocyte
95 morphological development. We identify that the WW-binding motif in NL2 is necessary
96 for astrocyte morphogenesis. Using an unbiased proximity-labeling approach *in vivo*, we
97 uncover interaction networks for astrocytic NL1, NL2, and NL3. We also performed
98 proximity-labeling for neuronal NL2 to compare cell-type specific differences in NL2
99 interactome and function. We show that NLs have distinct interactomes representing
100 unique functions within astrocytes and between astrocytes and neurons. These data
101 revealed numerous WW domain-containing proteins that recognize the WW-binding
102 motifs in NLs. Of these, we identified Nedd4l, a HECT-domain E3 ubiquitin ligase, to
103 control NL2 stability via ubiquitination, which is necessary for astrocyte morphogenesis.
104 Moreover, the loss of Nedd4l in astrocytes results in a stunted astrocyte morphology.

105 Importantly, Nedd4l interacts with NL1 and NL2, but not NL3. Together, this study
106 reveals unique interactions of astrocytic NL2, which reveal a novel mechanism of
107 astrocyte morphological development.

108

RESULTS

Astrocytic Neuroligins 1, 2, and 3 have non-redundant roles in morphogenesis.

NLs 1, 2, and 3 are all expressed throughout development in mouse cortical astrocytes(Boisvert et al., 2018; Clarke et al., 2018; Zhang et al., 2014; Farhy-Tselnicker et al., 2021). Previous work from our lab demonstrated that loss of either NL1, NL2, or NL3 from cortical astrocytes significantly reduces astrocyte complexity. Moreover, the loss of all three NLs simultaneously results in an additive reduction of complexity(Stogsdill et al., 2017), indicating that these proteins play distinct roles during astrocyte development. NLs have similar ECD amino acid sequences yet differ substantially in their intracellular domains (Fig 1A). Considering the differences in amino acid sequence and the combinatorial deficit in astrocyte complexity, we analyzed whether NLs have redundant roles in astrocyte morphogenesis. To address this question, we used an optimized and validated *in vitro* astrocyte-neuron co-culture method to quantify astrocyte branch complexity via Sholl analysis(Stogsdill et al., 2017; Baldwin et al., 2021; Tan et al., 2023) (Fig 1B). Previously, we showed that astrocytes require neuronal contact to develop a highly branched morphology(Baldwin et al., 2021; Stogsdill et al., 2017). In this system, we can manipulate astrocyte gene expression without affecting the neurons. We focused on NL2 because the loss of NL2 affects astrocyte morphogenesis *in vivo* at both early and late developmental time points, suggesting a critical role for astrocytic NL2. We transfected astrocytes with a plasmid expressing an shRNA for *Nlgn2* (shNL2) which has been extensively used and tested for off-target effects(Stogsdill et al., 2017; Chih et al., 2006; Singh et al., 2016). This plasmid also encodes CAG-GFP to visualize transfected cells. Loss of *Nlgn2* in

132 astrocytes causes a substantial reduction in astrocyte morphology when co-cultured
133 with neurons (Fig S1A, B; Fig 1C, D). To provide another line of evidence for the role of
134 Nlgn2 in astrocyte morphogenesis and address potentially confounding results due to
135 shRNA toxicity(Goel and Ploski, 2022), we designed and tested gRNAs targeting rat
136 *Nlgn2* (Fig S1C). Two of three of the gRNAs targeting *Nlgn2* were able to cause a
137 translation-disrupting frameshift mutation, reflected by the loss of GFP expression
138 downstream of the gRNA and PAM sequences (see Methods) (Fig S1D). We expressed
139 these two gRNAs in primary rat astrocytes, along with *Staphylococcus aureus* Cas9
140 (SaCas9)(Hunker and Zweifel, 2020), under the control of the GfaABC1D promoter(Lee
141 et al., 2008) and found that both gRNAs significantly reduced the morphological
142 complexity in transfected astrocytes cultured with WT neurons, compared to the empty
143 vector control (Fig S1E, F). Thus, these data further support that our Nlgn2 shRNA is
144 specific, and the morphological phenotype cannot be explained by cytotoxicity.

145 Next we tested whether the stunted morphological phenotype of *Nlgn2* knockdown
146 astrocytes can be rescued by the co-expression of an HA-tagged NL2 that has been
147 modified to be shNL2 resistant (HA-NL2-RM)(Stogsdill et al., 2017) or via the co-
148 expression of HA-tagged NL1 or NL3 with shNL2. Interestingly, HA-tagged NL1 or NL3
149 did not rescue the astrocyte morphology (Fig 1C, D). In contrast, co-expression of HA-
150 NL2 with either shNL1 or shNL3 curiously resulted in a higher number of maximum
151 intersections in the astrocyte branches compared to a scrambled shRNA control (shCtrl)
152 (Fig 1E, F). Together, these data show that NLs 1, 2, and 3 do not have redundant roles
153 in controlling astrocyte morphogenesis. Moreover, these findings suggest that NL2 is
154 indispensable in astrocyte morphological development.

155 **The intracellular WW-binding motifs of Neuroligins uniquely regulate astrocyte**
156 **morphology**

157 Previous work has revealed unique roles for the NL ICD in controlling synaptic
158 transmission(Nguyen et al., 2016). Thus, we hypothesized that the ICDs of NLs may
159 underlie their distinct roles in controlling astrocyte morphogenesis. NLs contain multiple
160 protein motifs in their ICDs (Fig S2A) that regulate binding to synaptic scaffolding
161 molecules, including Gephyrin and Collybistin(Poulopoulos et al., 2009) which are
162 necessary for inhibitory synapse specification, and PSD-95(Irie et al., 1997), which
163 organizes excitatory postsynaptic sites. We wondered if any of these motifs in the NL2
164 ICD are necessary for astrocyte morphology. We used mutagenesis to either delete the
165 NL2 PDZ binding domain (NL2 ΔPDZ, deletion of amino acids 833-836), or the NL2
166 polyproline-rich motif, which activates Collybistin (NL2 ΔPRM, deletion of amino acids
167 798-805) or mutate NL2 Gephyrin binding residue (NL2 GBM, Y770A) (Fig 2A). We
168 tested whether these mutant constructs could rescue the shNL2 morphological deficits
169 in our co-culture system. These mutants do not alter NL2 localization, as all mutants
170 were trafficked to the cell surface (Fig S2B). Surprisingly, all three mutants were able to
171 rescue the morphological deficits in shNL2 astrocytes (Fig 2B-C), suggesting that
172 potential interactions with Gephyrin, Collybistin, and PSD-95 are dispensable for NL2
173 control of astrocyte morphology.

174 To identify the regions of the NL2 ICD that are required for astrocyte morphogenesis,
175 we used previously validated(Nguyen et al., 2016) NL2 chimeric constructs to
176 investigate whether replacing the NL2 ICD with either the NL1 or the NL3 ICD is
177 sufficient to rescue the loss of NL2 in astrocytes (Fig 2D). Using astrocyte-neuron co-

178 cultures, we expressed the NL chimeras in astrocytes in the presence of shNL2 and
179 quantified astrocyte complexity (Fig 2E). While the NL2 ECD/NL1 ICD condition resulted
180 in more complex astrocytes than shNL2 alone, the astrocytes transfected with NL2
181 ECD/NL3 ICD were identical to shNL2 alone (Fig 2F). This finding suggests that NL1
182 and NL2 ICD share a common amino acid sequence necessary for controlling astrocyte
183 morphogenesis, which is absent from the NL3 ICD.

184 To pinpoint the interaction motif in the NL2 ICD that is required for astrocyte
185 morphogenesis, we aligned the intracellular domain amino acid sequences of NL1-3
186 (Fig 2G, Fig S2A) and isolated motifs that were present in both NL1 and NL2, but
187 absent from NL3. Using TomTom motif scanning(Gupta et al., 2007), we found the
188 sequence PPDY – a Group I WW domain binding motif, known to have the consensus
189 sequence of PPxY(Kasanov et al., 2001; Pirozzi et al., 1997), to fit our criterion. When
190 we mutated the PPDY motif of NL2 ICD to four alanines, this mutant could no longer
191 fully support astrocyte morphogenesis (Fig 2H-J). Similarly, mutation of the PPDY
192 (PPDY > AAAA) in the NL2 ECD/NL1 ICD chimera completely ablated the
193 morphogenesis rescue previously seen for the non-mutated chimera (Fig 2H-J).
194 Together, these data suggest that NL2 controls astrocyte morphogenesis through
195 interactions mediated via the PPDY motif in its ICD.

196 ***In vivo* BioID reveals unique interactions of astrocytic Neuroligins, including WW**
197 **domain-containing proteins**

198 PPxY motifs are recognized by Group I WW domain-containing proteins(Kato et al.,
199 2004, 2002). WW domains are around 40 amino acids, with two flanking conserved
200 tryptophan (single amino acid code: W) residues(Sudol and Hunter, 2000). In the

201 human proteome, there are over 50 proteins that contain a WW domain, with many
202 proteins containing multiple WW domains. To identify which WW domain-containing
203 protein binds NL1 and NL2, we used *in vivo* BioID (iBioID). This approach(Roux et al.,
204 2012) uses a biotin ligase, Turbo BirA, fused to a bait protein to identify all proteins
205 interacting with the bait, within 10nm(Branon et al., 2018). We made C-terminal fusions
206 of Turbo BirA to NL1, 2, or 3 and virally expressed these constructs under the control of
207 the astrocyte promoter GfaABC1D(Lee et al., 2008) (Fig 3A-D). To investigate cell-type
208 specific differences in NL2 interactome, we also expressed NL2-Turbo BirA under the
209 control of the neuronal promoter hSyn1 (Fig 3A-B). As controls, we expressed soluble
210 TurboID in astrocytes or neurons, which will biotinylate the repertoire of intracellular
211 proteins in each cell-type. We chose to use a cytosol-localized control, as NLs are
212 trafficked throughout many cellular compartments(Kang et al., 2014; Binda et al., 2019;
213 Halff et al., 2019; Xie et al., 2023; Xu et al., 2024) , and we aimed to capture all
214 physiologically relevant interactors, not just those at the plasma membrane. We
215 confirmed that the NL2-Turbo BirA constructs were properly localized to the cell
216 membrane in cultured astrocytes (Fig S3A) and they could rescue the morphological
217 deficits of shNL2 astrocytes (Fig S3B, C), thus indicating that NL2 functioned as
218 expected. However, we found that placing the Turbo BirA after the PDZ binding motif in
219 the NL2 C-terminal diminished the biotinylation activity of the enzyme. Thus, we moved
220 the PDZ domain after the TurboID. We could see robust biotinylation after moving the
221 Turbo BirA to just before the PDZ binding motif (Fig S3B) and proceeded with this
222 placement of the TurboID (before the PDZ binding motif) for all NL constructs (Fig 3A).

223 We injected perinatal mice (P0-P1) intracortically with AAVs expressing the NL-Turbo
224 BirA fusions, or the cell-type-specific soluble BirA control. After three days of biotin
225 injection (P18-P20), we collected P21 mouse cortices and isolated biotinylated proteins
226 by streptavidin immunoprecipitation (Figs 3A, E). We chose P21 as an endpoint
227 because NL2 loss in developing astrocytes results in significantly smaller astrocyte
228 territories with concomitant deficits in synapse formation and function at P21(Stogsdill et
229 al., 2017). We confirmed that our viral vectors were cell-type-specific by staining for the
230 astrocyte-specific marker Sox9 (Fig 3C-D) or the neuronal-specific marker NeuN (Fig
231 S3D), and both induced cell-type-specific biotinylation (visualized by Streptavidin-594
232 antibody staining) *in vivo*. Mass spectrometry identification and quantification of the
233 biotinylated proteins (Fig S4 A-D, Dataset S1) revealed substantial differences in the
234 putative interactomes of astrocytic NL1-3 (Fig 3F, Dataset S1), when normalized to their
235 respective soluble TurboID controls. Similarly, there were substantial differences
236 between proteins proximal to neuronal versus astrocytic NL2 (Fig 3F, Dataset S1).

237 We bioinformatically compared our data to previously published NL2 interactome data
238 (identified via NL2 co-immunoprecipitation in adult mouse whole brain(Kang et al.,
239 2014), *in vitro* extracellular NL2 APEX proximity proteomics(Loh et al., 2016), and a
240 yeast two-hybrid screen of the NL2 ICD(Poulopoulos et al., 2009)) and found a
241 significant overlap with our datasets for each of the previously published data (Fig 4A).
242 We also found noticeable differences between the astrocytic and neuronal interactome
243 of NL2. For example, neuronal NL2 is well characterized to interact with the inhibitory
244 synapse scaffold protein, Gephyrin(Poulopoulos et al., 2009), which we detected to be
245 highly enriched in the neuronal NL2 iBioID interactome (Fig 4B, Dataset S1). However,

246 even though Gepyhrin is present in astrocytes at both the mRNA(Zhang et al., 2014)
247 and protein levels (Dataset S1), we did not detect a significant enrichment of Gepyhrin
248 in the astrocytic NL2 iBioID (Fig 4B, Dataset S1). This result strongly suggests cell-type-
249 specific regulation of protein-protein interactions of NL2 and is consistent with our
250 finding that Gephyrin interaction with NL2 is not necessary for astrocyte morphogenesis
251 (Fig 2A, B).

252 Gene ontology analysis of the unique proximity interactomes across astrocytic NLs
253 suggests distinct functions of NLs in astrocytes (Fig 4C) and of astrocytic vs neuronal
254 NL2 (Fig 4D). For example, while all astrocytic NLs interact with ion channels and solute
255 transporters, astrocytic NL1 alone interacts with proteins involved in epigenetic
256 modifications, while astrocytic NL2 proximal proteins appear to bind phospholipids.
257 These data support our earlier findings, showing that NLs have non-redundant roles in
258 astrocytes and that these differences likely extend beyond the control of astrocyte
259 morphogenesis. Further, gene ontology analysis of NL2 proximal proteins between
260 neurons and astrocytes reveals functional differences. Interestingly, only astrocytic NL2
261 interacts with proteins that bind actin filaments (Fig 4D, S4E), which are abundant in
262 perisynaptic astrocyte processes(Soto et al., 2023).

263 The putative NL2 interactome we identified provided us with the means to determine
264 which nearby proteins could recognize the PPxY motif in NL2 and thus participate in
265 NL2-controlled astrocyte morphogenesis. To do so, we analyzed WW domain-
266 containing proteins across all datasets that were significantly enriched with the bait
267 protein, compared to the cytoplasmic control. Across the 4 iBioID experiments, we
268 found 9 WW domain-containing proteins within NL interactomes (Fig 4E). The WW

269 domain-containing proteins within the NL interactomes varied across NL isoform and
270 cell type. Even though NL1 and NL2 have identical PPxY motifs (PPDY, Fig 2G), there
271 was minimal overlap in WW domain-containing proteins that interacted with both. This
272 finding suggests that the interactions of NLs with WW domain-containing proteins in
273 vivo are not solely determined by the presence of the PPxY motif, and that additional
274 protein-protein interaction motifs in the ICD may confer specificity to these interactions.
275 Furthermore, the utility of including NL3 as a bait in our BioID experiments served as an
276 informative control for the PPxY motif, as NL3 contains the LPxY motif, which is only
277 weakly bound by WW proteins, providing a strong comparative reference for motif-
278 dependent interactions.

279 **The WW domain-containing E3 ubiquitin ligase Nedd4l is necessary for astrocyte**
280 **morphogenesis, but not synaptogenesis**

281 The binding of WW domains to WW motifs has various physiological effects in the cell
282 including cellular growth(Lee et al., 2020), endocytosis of membrane proteins(Totland et
283 al., 2017), and transcription(Sudol et al., 2001). Importantly, WW domain-containing
284 proteins and their interactions with WW motifs have been implicated in various
285 diseases, including the neurodevelopmental disorder Rett Syndrome(Rodrigues et al.,
286 2020), Muscular Dystrophy(Ilsley et al., 2002), and hypertension(Minegishi et al., 2016).
287 We observed three significantly enriched WW domain-containing protein interactors of
288 astrocytic NL2, Dystrophin (*Dmd*), growth arrest-specific protein 7 (*Gas7*), and neural
289 precursor cell expressed developmentally downregulated 4-like protein (*Nedd4l*, also
290 called Nedd4-2) (Fig 4E). We chose to focus on Nedd4l from these results for two
291 reasons. First, both NL1 and NL2 PPDY motifs are necessary for astrocyte

292 morphogenesis (Fig 2I-J), and Nedd4l is enriched in astrocytic NL1 and NL2, but not
293 NL3 (Fig 4E) proximity proteomes. Second, Nedd4l has a known role in regulating
294 astrocyte membrane proteins. For example, Nedd4l controls the abundance of the
295 potassium channel Kir4.1, the gap junction protein, Connexin-43(Altas et al., 2024; Liu
296 et al., 2021) as well as the abundance and surface localization of the glutamate
297 transporter Glt-1(Zhang et al., 2017), via ubiquitination.

298 To investigate if Nedd4l is necessary for astrocyte morphogenesis, we designed and
299 validated an shRNA (Figs 5A, S5A-B) targeting *Nedd4l*. We expressed this shRNA in
300 astrocytes to determine how the loss of Nedd4l impacts the morphological complexity of
301 astrocytes cultured with wild-type neurons. Strikingly, we observed a severe reduction in
302 astrocyte morphological complexity in shNedd4l-transfected astrocytes, compared to
303 control (Fig 5A-B). Co-knockdown of *Nedd4l* and *Nlgn2* (using a plasmid that also
304 encodes mCherry) did not further reduce astrocyte complexity. These findings suggest
305 that Nedd4l and NL2 might work in the same pathway (Fig 5B).

306 Next, we tested whether Nedd4l is necessary for astrocyte morphogenesis *in vivo*. To
307 achieve genetically targeted and sparsely labeled astrocytes in the mouse cortex, we
308 used postnatal astrocyte labeling by electroporation (PALE)(Baldwin et al., 2021;
309 Stogsdill et al., 2017). In this method, plasmid DNA expressing a shRNA with
310 CAG:mCherry-CAAX and a GLAST promoter-driven piggyBac enzyme are injected into
311 P0-P1 mouse lateral ventricles and then electroporated into the cortex. This technique
312 results in the uptake of the plasmid by radial glia and subsequent astrocyte labeling
313 after differentiation (Fig 5C). Using this technique, we previously found that loss of
314 astrocytic NL2, using both shRNA targeting *Nlgn2* or a floxed allele with astrocytic Cre

315 expression, results in a significantly stunted astrocyte territory volume and branch
316 complexity(Stogsdill et al., 2017). We used confocal imaging of the entire astrocyte in
317 100µm tissue sections and reconstructed the astrocyte volume using Imaris software.
318 Quantification of the astrocyte territory volume revealed a significant reduction in
319 shNedd4l astrocytes, compared to a scrambled shRNA control (shCtrl) (Fig 5D-E).
320 Additionally, quantification of the astrocyte complexity using *in vivo* Sholl analysis
321 revealed a significant decrease in complexity of Nedd4l knockdown astrocytes (Fig 5F).
322 These data suggest that astrocyte morphogenesis is controlled by Nedd4l at both the
323 level of territory size and branch complexity.

324 We previously showed that loss of *Nlgn2* in sparsely labeled astrocytes in the mouse V1
325 cortex results in reduced excitatory synaptogenesis in the surrounding neuropil. Thus,
326 next, we tested if Nedd4l loss also affects synapse density by using PALE to knock
327 down *Nedd4l* in sparse astrocytes in the mouse V1 cortex. At P21, we stained cortical
328 sections for presynaptic Bassoon, and postsynaptic PSD95 and Gephyrin. Using a
329 combination of these antibodies, we quantified both excitatory (closely apposed
330 Bassoon and PSD95) and inhibitory (Bassoon and Gephyrin) synapses in the same
331 sections (Fig S6B). We used the mCherry signal from the piggyBAC vector (Fig 5C) to
332 define perturbed astrocyte territories. Using open-source SynBot software(Savage et
333 al., 2024), we quantified the synaptic density within labeled astrocytes and outside of
334 labeled astrocytes (Fig S6A-B). These data revealed no significant differences in
335 synapse density in *Nedd4l*-knockdown astrocytes, *in vivo* (Fig S6C-D). This data
336 suggests Nedd4l and its interaction with NL2 controls astrocyte morphological
337 development independently from the role of astrocytic NL2 in synaptogenesis. Thus, the

338 WW domain-containing protein Nedd4l is necessary for astrocyte morphogenesis, but
339 not for astrocyte-dependent synaptogenesis.

340 **The PPDY motif in Neuroligin-2 is sufficient for Nedd4l interaction**

341 The Nedd4 family is part of Group I WW binding proteins, which exhibit preferential
342 binding to PPxY motifs and only weakly bind to LPxY(Hatstat et al., 2021). In the
343 absence of a PPxY containing substrate, Nedd4l is known to bind its own LPxY motif,
344 autoubiquitinate and degrade(Bruce et al., 2008). Because NL1 and NL2 have a PPxY
345 motif, and NL3 has an LPxY motif (Fig 2G; Fig S2B), we wondered if Nedd4l
346 preferentially and directly interacted with NL1 and NL2 ICDs but not the NL3 ICD. To
347 test this, we used either the wildtype NL2 or NL2 ECD/NL1 ICD chimeras (Fig 2D) and
348 mutated the NL2 ICD and NL1 ICD PPDY motifs to alanines to abolish the WW domain-
349 containing motif, as described earlier (Fig 2H-J; Fig 6A). Conversely, we also mutated
350 the NL3 ICD LPDY motif to PPDY to mimic NL1 and NL2 ICDs. All chimeric constructs
351 contained the NL2 ECD to rule out the effects of sequence divergence in NL ECDs.

352 Next, we co-expressed HA-tagged NL2 and NL2 chimeras with V5-tagged Nedd4l in
353 HEK 293T cells and co-immunoprecipitated NLs using anti-HA tag magnetic beads. We
354 found that Nedd4l co-immunoprecipitated with wildtype NL2 (Fig 6B); however, ablation
355 of the PPDY motif in NL2 ICD (NL2ΔWW, Fig 6A) resulted in a substantial, yet variable,
356 reduction of Nedd4l co-immunoprecipitation (Fig 6B, C). A previous study investigating
357 the interaction of NL2 and the WW domain-containing protein S-SCAM (*Magi2*) found
358 that a longer stretch of amino acids 766-796, which contains the PPDY motif, in the NL2
359 ICD is necessary for direct binding of S-SCAM to NL2(Sumita et al., 2007). Thus, we
360 next deleted these amino acids from the NL2 ICD (NL2ΔWWLrg, Fig 6A) and performed

361 co-immunoprecipitation with Nedd4l. Loss of this sequence in NL2 ICD completely
362 abolished the interaction with Nedd4l (Fig 6D-E), demonstrating that this is a critical
363 region in NL2 ICD containing the PPDY motif that mediates Nedd4l binding.

364 Ablation of the PPDY motif in NL1 ICD (NL2/1ΔWW, Fig 6A), however, abolished the
365 interaction with Nedd4l entirely, further showing the importance of the PPDY motif in
366 NL-Nedd4l interactions (Fig 6F-G). As expected, we found that Nedd4l does not interact
367 with wild-type NL3 ICD (Fig 6H). However, strikingly, mutating the LPDY motif of NL3
368 ICD to PPDY (NL2/3WW, Fig 6A, H-I) was sufficient to induce an interaction between
369 Nedd4l and NL3 ICD. These results reveal that the PPDY is sufficient for Nedd4l
370 interactions with NL ICDs. Additional sequences in the NL2 ICD between amino acids
371 766-796 flanking the PPDY motif are also involved in NL2/Nedd4l binding.

372 **Nedd4l ubiquitinates Neuroligin-2 at K749, resulting in increased stability of**
373 **Neuroligin-2**

374 Nedd4l is an E3 ubiquitin ligase of the HECT domain family which has previously been
375 shown to polyubiquitinate the astrocyte membrane proteins Kir4.1, Connexin-43, and
376 Glt-1, resulting in their degradation(Altas et al., 2024; Liu et al., 2021; Zhang et al.,
377 2017). Previous proteomic studies have identified that the intracellular domain of NL2 is
378 ubiquitinated at lysine 749 (K749)(Na et al., 2012; Wagner et al., 2012) in both mouse
379 and rat brain tissues. However, the function of this posttranslational modification in NL2
380 is unknown. Thus, next, we investigated whether NL2 is ubiquitinated at K749. To do
381 so, we first blocked proteasomal degradation using the proteasomal inhibitor MG-132.
382 We next heat-denatured lysates to disrupt protein-protein interactions and subsequently
383 immunoprecipitated HA-NL2 from primary rat astrocytes. After running the

384 immunoprecipitated eluates on a western blot, we found that HA-NL2 showed a smear
385 of high molecular weight HA-immunoreactive protein, indicative of polyubiquitinated
386 protein (Fig 7A). We found that we could significantly decrease this polyubiquitination by
387 mutating K749 to R (Arginine), as immunoprecipitation of HA-NL2K749R primarily
388 displayed only one band at the expected molecular weight for NL2 (Fig 7A-B). These
389 data show that NL2 is ubiquitinated in primary astrocytes, which can be blocked by
390 mutating K749.

391 We next aimed to test if Nedd4l ubiquitinates NL2. Interestingly, while our *Nedd4l*
392 expression construct works well in HEK 293T cells, we were unable to overexpress
393 Nedd4l in primary astrocytes. This may be due to global proteasome disruptions and
394 cytotoxicity due to Nedd4l's role in astrocyte protein turnover(Altas et al., 2024). To
395 circumvent this, we turned to HEK 293T cells and expressed HA-NL2 with or without
396 V5-Nedd4l co-expression and then probed for GFP-tagged ubiquitination via Western
397 blot with a GFP antibody. We found that, indeed, compared to NL2 alone, co-expression
398 with Nedd4l resulted in a high molecular weight smear above the expected size of NL2
399 indicating that Nedd4l is sufficient to enhance polyubiquitination of NL2, when compared
400 to NL2 alone (Fig S7A-B). Further, we could reduce this ubiquitination by mutating K749
401 of NL2 to arginine (K749R). Co-expression of Nedd4l and NL2K749R also did not result
402 in enhanced polyubiquitination of NL2, indicating that K749 is the only ubiquitinated
403 residue in NL2 (Fig S7A-B). Together, these data reveal that Nedd4l is sufficient to
404 ubiquitinate NL2 at K749.

405 While ubiquitination is typically associated with protein degradation, it can also serve as
406 a posttranslational signal for various cellular processes(Mukhopadhyay and Riezman,

407 2007). We first tested whether Nedd4l-mediated ubiquitination of NL2 results in the
408 degradation of NL2. We expressed NL2 with or without Nedd4l in HEK cells and
409 collected cell lysates at different time points after cycloheximide (CHX) treatment, which
410 blocks nascent translation. Western blotting of these samples revealed a decrease in
411 HA-NL2 abundance over time, indicating NL2 is degraded (Fig 7C-D). Strikingly, co-
412 expression of Nedd4l with NL2 completely blocked this degradation and stabilized NL2
413 protein over time (Fig 7C-D). Interestingly, mutation of NL2 lysine 749 to arginine
414 (K749R) was sufficient to block NL2 degradation, with no further effect by the addition of
415 Nedd4l (Fig 7E-F). Taken together, these data reveal that ubiquitination at K749
416 controls NL2 degradation; however, ubiquitination at K749 by Nedd4l stabilizes NL2
417 protein and prevents its degradation.

418 **Ubiquitination of Neuroligin-2 at Lysine 749 is required for astrocyte**
419 **morphogenesis**

420 NL2 is ubiquitinated, *in vivo*(Na et al., 2012; Wagner et al., 2012), yet whether
421 ubiquitination at this residue has a functional role is unexplored. Therefore, we next
422 tested if ubiquitination at K749 is necessary for NL2's control of astrocyte
423 morphogenesis. To do so, we expressed NL2K749R (also mutated to be resistant to
424 shNL2) in primary astrocytes and subsequently co-cultured the astrocytes on top of
425 neurons to quantify astrocyte complexity. Surprisingly, we found that NL2K749R
426 expression significantly reduced astrocyte morphology in a dominant-negative fashion
427 compared to the scrambled shRNA control (Fig 8A-B). NL2K749R was also incapable of
428 any morphological rescue of shNL2 transfected astrocytes (Fig 8A-B).

429 Finally, we investigated whether NL2K749R is crucial for astrocyte morphogenesis in
430 the developing mouse cortex. In *Nlgn2* homozygous flox animals (*Nlgn2* $^{fl/fl}$), also
431 carrying a Rosa26:lox-STOP-lox tdTomato allele, we used PALE (Fig 5C), to express
432 Cre to ablate *Nlgn2* in astrocytes, while simultaneously expressing HA-NL2 (WT) or HA-
433 NL2K749R (Fig 8C). At P21, we harvested the brains to analyze astrocyte
434 morphological development via Imaris reconstruction and 3D Sholl analysis. As
435 previously shown(Stogsdill et al., 2017), the knock-out of both copies of *Nlgn2* via Cre
436 expression in astrocytes results in a significantly diminished territory volume, compared
437 to *Nlgn2* $^{+/+}$ animals (also carrying the Rosa26:lox-STOP-lox tdTomato allele) (Fig 8D).
438 This morphological deficit was rescued by co-expressing an HA-tagged NL2 plasmid in
439 the astrocytes (Fig 8D). Supporting our *in vitro* findings (Fig 8B), co-expression of HA-
440 NL2K749R with Cre in *Nlgn2* $^{fl/fl}$ astrocytes was not able to rescue the reduction in
441 territory volume, and showed no significant difference between *Nlgn2* $^{fl/fl}$ astrocytes that
442 received Cre alone (Fig 8D). We did observe a bimodal distribution in the territory
443 volumes of *Nlgn2* $^{fl/fl}$ astrocytes that received Cre + HA-NL2K749R that was not related
444 to sex or astrocyte layer identity, suggesting an unknown variable influences the
445 functional importance of NL2 ubiquitination status. Further, we found that astrocyte
446 complexity, measured by 3D Sholl analysis (Fig 8E), largely mirrored the territory
447 volume findings in Fig 8D. Altogether, these findings show that ubiquitination of NL2 at
448 K749 is necessary for its role in astrocyte morphogenesis at both the territory volume
449 and branch complexity levels.

450 **DISCUSSION**

451 Astrocytes play crucial roles in nervous system development and function. Proper
452 astrocyte function relies on their highly branched astrocyte morphology, which is largely
453 controlled by cell-adhesion molecules(Ackerman et al., 2021; Baldwin et al., 2021;
454 Stogsdill et al., 2017; Tan et al., 2023). However, the mechanisms downstream of these
455 cell adhesion molecules are not yet fully understood. Here, we show that NLs are non-
456 redundant in controlling astrocyte morphology due to their unique intracellular protein
457 interactomes. We found a critical motif that regulates Nedd4l interaction and
458 ubiquitination of NL2, which is necessary for NL2-mediated control of astrocyte
459 morphogenesis. Further, we provide *in vivo* astrocytic NL1-3 and neuronal NL2
460 proximity proteomes, which provide insights into the differences in astrocytic NL function
461 and cell-type-specific functions of NL2 between astrocytes and neurons.

462 How do NLs uniquely contribute to astrocyte morphogenesis? We found that
463 overexpression of NLs could not compensate for the loss of one another *in vitro*, which
464 may be explained by various reasons. First, NL mRNA expression patterns differ in the
465 developing cortex(Clarke et al., 2018), suggesting that temporal dynamics of NLs may
466 differentially control astrocyte cytoarchitecture. Second, NLs form both homo- and
467 heterodimers, and dimerization is necessary for both localization and
468 function(Poulopoulos et al., 2012; Shipman and Nicoll, 2012). In neurons, only NL1/NL3
469 and NL1/NL2 heterodimers have been detected(Poulopoulos et al., 2012); however, our
470 results indicate that both NL1/NL2 and NL2/NL3 dimers exist in both astrocytes and
471 neurons, suggesting that cell-type-specific heterodimers may impact NL function during
472 brain development. Lastly, our interactome data reveals disparate protein interactions

473 with NLs which likely contribute to unique astrocytic NL function. Interestingly, gene
474 ontology analysis revealed a significant interaction with actin binding proteins and
475 cytoskeletal related proteins specifically for astrocyte NL2, and minimally for astrocyte
476 NL1 or NL3 or neuronal NL2, suggesting astrocytic NL2 plays a unique role in
477 controlling astrocyte morphology (Dataset S2, Fig S4 E-F). However, it is important to
478 note a few limitations of our iBioID data: first, because the TurboID promiscuously
479 biotinylates proteins within 10nm, interactions with a bait protein (here, NLs) may or
480 may not be due to direct binding and should be validated orthogonally, as we showed
481 with Nedd4l (Fig 6). Second, interactions with NLs may be transient and/or
482 developmentally regulated, and thus, our 3-day biotinylation treatment window may
483 capture both static and transient interactions. Therefore, these data should not be
484 interpreted as a compendium of NL-interacting proteins. Lastly, GFAP promoter activity
485 is highest in the lower layers of the cortex (Fig 3C-D), thus our astrocyte-specific
486 proteomic experiments are largely influenced by lower-layer astrocytes. Nevertheless,
487 the iBioID interactomes generated in this study will be beneficial in elucidating the
488 mechanisms through which NLs control astrocyte structure and function.

489 In this work, we show that the WW domain-containing protein Nedd4l is critical for
490 astrocyte morphogenesis, and this protein has distinct specificity for each NL, which we
491 validated by direct protein-protein interaction. How do WW domain proteins specify
492 interactions with NLs? Nedd4l preferentially binds PPxY motifs, but can also weakly
493 bind LPxY(Bruce et al., 2008; Hatstat et al., 2021). We identified that NL1 and NL2
494 contain a PPxY motif in their ICDs, whereas NL3 contains an LPxY motif. This single
495 amino acid change ultimately impacts the binding of Nedd4l to NLs but does not explain

496 the interaction specificity entirely. Only after deleting amino acids 766-796 in NL2, ICD
497 Nedd4l binding is blocked, suggesting a larger surface is critical for the interaction
498 between NL2 and Nedd4l. This may explain why mutation of PPDY to AAAA in the NL2
499 ICD is still able to restore some of the astrocyte complexity (Fig 2J) and suggests that
500 the WW binding motif in NL2 is not the sole determinant of NL2 function in astrocyte
501 morphogenesis. Moreover, in our iBioID results, Nedd4l is not enriched in NL1 proximal
502 proteome as strongly as NL2 in astrocytes, which may indicate a weaker physiological
503 interaction. Tyrosine phosphorylation in WW motifs is known to occlude binding with
504 WW domains(Chen et al., 1997). The conserved Tyrosine (Y) in the PPxY motif is the
505 same residue that modulates Gephyrin binding (Y770)(Poulopoulos et al., 2009) and is
506 phosphorylated in neuronal NL1 but not neuronal NL2(Letellier et al., 2018), therefore,
507 phosphorylation and/or Gephyrin binding might modulate Nedd4l binding to NLs. Nedd4l
508 interactions with its known targets are controlled through adapter proteins, namely the
509 14-3-3 family(Lee et al., 2018; Nagaki et al., 2006). Our data reveals that astrocytic NL2
510 interacts with several of the 14-3-3 family proteins, pointing toward a role of 14-3-3
511 proteins mediating the Nedd4l-NL2 interaction in astrocytes. Moreover, several WW
512 domain-containing proteins interact with NLs in a cell-type-specific manner (Fig. 4E).
513 Future studies will reveal the cell-type-specific effects of WW domain-containing protein
514 interactions with NLs.

515 Until this study, the functional consequence of NL2 ubiquitination had not been
516 demonstrated in either astrocytes or neurons. We found that Nedd4l ubiquitinates NL2
517 at K749. Numerous reports indicate that Nedd4l ubiquitinates its targets, including the
518 astrocytic targets Kir4.1 and Connexin-43(Altas et al., 2024), which results in

519 proteasome-mediated degradation(Liu et al., 2021; Zhang et al., 2017; Zhou et al.,
520 2007). However, here we found that Nedd4l ubiquitination of NL2 results in increased
521 stability of NL2. Interestingly, ubiquitination-mediated protein stabilization has been
522 reported previously for other HECT E3 ubiquitin ligases. Nedd4, a close family member
523 of Nedd4l, has been demonstrated to ubiquitinate another E3 ubiquitin ligase, Mdm2,
524 which results in increased stability of the protein(Xu et al., 2015). We speculate that
525 Nedd4l-mediated stability of NL2 may maintain the surface pool of NL2 and/or overall
526 NL2 abundance, to maintain synaptic contacts with Neurexins. While Nedd4l
527 ubiquitination of NL2 does not lead to protein degradation, our data reveal that
528 NL2K749 ubiquitination can be a degradative signal. In heterologous cells, NL2 protein
529 abundance significantly decreases over time, and blocking ubiquitination at K749
530 prevents this degradation (Fig 7C-F). A limitation of this experiment is that it was
531 performed in heterologous cells, due to the low expression, possibly resulting from rapid
532 degradation, of astrocytic NL2 in the absence of neurons. Future work using cell-type-
533 specific knock-in or conditional degradation models will be required to test Nedd4l's role
534 in regulating NL2 stability in astrocytes, *in vivo*. Finally, ubiquitination of NL2 was
535 identified in both mouse and rat brains at lysine K749 via ubiquitin proteomics, but NL1
536 and NL3 were not(Na et al., 2012; Wagner et al., 2012). We found that blocking
537 ubiquitination at K749 results in a stunted morphological phenotype for NL2-mediated
538 astrocyte morphogenesis, both *in vitro* and *in vivo* (Fig 8A-E). This phenotype may be
539 due to an excess of NL2 in the astrocyte surface, thus leading to improper targeting of
540 perisynaptic astrocyte processes in the neuropil and preventing precise interactions with
541 neuronal neurexins. To this end, understanding how trans-synaptic neurexin binding to

542 NL2 impacts Nedd4l interaction with NL2 and/or ubiquitination of NL2 will be an
543 important future direction. Altogether, this finding underscores the importance of NL2
544 turnover in the development of astrocyte morphology.

545 Emerging evidence emphasizes the differential roles of astrocytic versus neuronal NLs.
546 Numerous laboratories have identified a unique physiological role of NLs in various glia
547 including astrocytes(Stogsdill et al., 2017; Ackerman et al., 2021), oligodendrocyte
548 precursor cells(Li et al., 2024), as well as glioma(Venkatesh et al., 2015, 2017).
549 Recently, an article claimed that astrocytic NLs do not control astrocyte morphogenesis
550 or synapse formation(Golf et al., 2025). This study used an astrocyte Cre line and floxed
551 NL alleles to knock out *Nlgns1-3* in the mouse brain, yet analyzed effects at different
552 timepoints than our study. First, the authors demonstrate a decrease in astrocyte-
553 specific ribosome-bound mRNA only at 8 weeks postnatally, but show no difference in
554 mouse cortical astrocyte morphology at P35. We suspect that their incongruous findings
555 are due to incomplete knock-down of NLs early in development, which we have
556 previously shown to be particularly difficult to knock out *in vivo* using the traditional Cre-
557 Lox system(Stogsdill et al., 2017). In this work, to circumvent such issues, we have
558 used carefully validated shRNAs(Chih et al., 2006) *in vitro* and *in vivo*, which have no
559 compounding effect in NL2 cKO astrocytes, indicating no off-target effects(Stogsdill et
560 al., 2017), and we have validated these findings using the CRISPR-Cas9 system (Fig
561 S1C-F) and PALE-mediated rescue of NL2-dependent astrocyte morphogenesis (Fig
562 8C-E). Further, our study lends insight into how slight perturbations of NL2 abundance,
563 in either direction, derail astrocyte morphology. We find that overexpression of NL2
564 does not completely rescue the morphological phenotype of shNL2 expressing

565 astrocytes (Fig S1B), suggesting that too much astrocytic NL2 results in an overly
566 adhesive phenotype. This aligns with the dominant negative morphological phenotype
567 of astrocytes expressing NL2 with the K749R mutation (Fig 8A-B), in which we expect
568 too much NL2 protein in the astrocytes due to the lack of proteasome-mediated
569 degradation of NL2 (Figure 7C-D).

570 In summary, we provide new insight into NL-mediated control of astrocyte
571 morphogenesis and reveal that the WW domain-containing protein, Nedd4l, is required
572 for astrocyte morphogenesis via ubiquitination and stabilization of NL2. Lastly, we show
573 that NL2 ubiquitination is critical for astrocyte morphogenesis, *in vitro and in vivo*.

574

575 **MATERIALS & METHODS**

576 **Mice**

577 All mice and rats were used in accordance with the Institutional Animal Care and Use
578 Committee (IACUC), under the guidance of the Duke Division of Laboratory Animal
579 Resources (DLAR) with protocol numbers A147-17-06, A117-20-05, and A103-23-04.
580 All animals were housed in 12-hour light/dark cycles. Timed-pregnant CD1 female mice
581 (RRID: IMSR_CRL:022) were used for PALE and iBioID experiments, obtained from
582 Charles River Laboratories. The NL2 floxed (B6;SJL-Nlgn2tm1.1Sud/J; Stock #025544,
583 RRID:IMSR_JAX:025544), and Ai14 (RTM) (B6;129S6-Gt(ROSA)26Sortm14(CAG-
584 tdTomato)Hze/J; Stock #007908, RRID:IMSR_JAX:007908) animals were obtained
585 through Jackson Laboratory. CD Sprague-Dawley IGS Rats (SD-001, RRID:
586 IMSR_CRL:400) were used for primary culture preps, obtained from Charles River
587 Laboratories. Mice and rats of both sexes were pooled and included in all experiments.

588 **Plasmids:**

589 *shRNA plasmids:*

590 shRNAs for NL1(RRID:Addgene_59339), 2 (RRID:Addgene_59358), and 3
591 (RRID:Addgene_59359) and scrambled NL shRNA control (shCtrl) constructs were
592 described previously(Stogsdill et al., 2017).

593 shRNAs were cloned into pLKO.1 vector (a kind gift from David Root, Addgene plasmid
594 #10878, RRID: Addgene_10878). A CAG-eGFP sequence was introduced into the
595 vector for expression in primary astrocytes. Antisense shRNA sequences:

596 ▪ Nedd4l: TTTATTAAGGGCTTTGCCTGC (Horizon Discovery, TRCN0000086868)

597 For PALE, the same shRNA sequence was cloned into a piggyBAC transposon system
598 expressing mCherry CAAX and transfected with a GLAST-piggyBACase plasmid (a kind
599 gift from Dr. Joseph LoTurco) as previously described(Tan et al., 2023). The Nedd4l
600 shRNA in the piggybac backbone is available at Addgene (RRID:Addgene_249589).

601 *NL chimeric plasmids:*

602 Chimeric HA-NL2 constructs were a kind gift from Dr. Roger Nicoll and described
603 previously(Nguyen et al., 2016) (NL2/1 Chimera RRID_Addgene_249601; NL2/3
604 Chimera RRID_249602). These constructs were modified to be resistant to
605 shNL2(Stogsdill et al., 2017).

606 *HA-NL2 mutation plasmids:*

607 Deletion of the PDZ domain (RRID:Addgene_249594), poly-proline domain
608 (RRID:Addgene_249595), and mutation of WW domains (PPDY → AAAA in NL2
609 (RRID:Addgene_249600), Large WW Deletion (a.a. 766-796 deletion,
610 RRID:Addgene_249599), PPDY → AAAA in NL1/2 chimera (RRID:Addgene_249597)
611 or LPDY → PPDY in NL3 chimera (RRID:Addgene_249598)) and K749R
612 (RRID:Addgene_249588) were performed using custom gene blocks (IDT) in the HA-
613 NL2-RM backbone. Mutation of the gephyrin binding residue in HA-NL2-RM (HA-NL2-
614 GBM-RM RRID:Addgene_249596) was performed via site-directed mutagenesis using
615 the QuikChange Lightning kit (Agilent) and the following primers:

616 Sense: 5' GCGCCCTGCCTGTgcagccGACgctACCCTGGCCTTGCGCCG 3'

617 Antisense: 5’ GCCCGGCGCAAGGCCAGGGTAGCGTCggctgcACAGGCAG 3’.

618 *TurboID plasmids:*

619 pZac2.1-gfaABC1D-Turbo-BirA plasmid was a kind gift from Dr. Scott Soderling. The
620 NL-Turbo fusion constructs were made by PCR amplification from the HA-tagged
621 expression plasmids and subsequent In-Fusion cloning (Takara). A flexible glycine
622 hexamer linker was inserted between the NL expression sequence and the Turbo-BirA.
623 pZac2.1-GFABC1D-Turbo-BirA was digested with XhoI and NotI to release the Turbo-
624 BirA to insert HA-NL1/2/3-Turbo-BirA. The gfaABC1D promoter was swapped for hSyn1
625 for neuronal expression of NL2-TurboID. The TurboID constructs are available through
626 Addgene: gfaABC1D HA-NL2 Turbo RRID:Addgene_249590; gfaABC1D HA-NL1 Turbo
627 RRID:Addgene_249591; gfaABC1D HA-NL3 Turbo RRID:Addgene_249592; hSyn1 HA-
628 NL2 Turbo RRID:Addgene_249593.

629 *Expression plasmids:*

630 HA-NL1 (RRID:Addgene_15227), HA-NL2 (RRID:Addgene_15259) and HA-NL3
631 (RRID:Addgene_59318) were previously described(Stogsdill et al., 2017). V5-Nedd4l
632 was made by custom geneblock cloning (IDT) from the HA-Nedd4l (human sequence, a
633 kind gift from Joan Massague (Addgene plasmid # 27000; RRID:Addgene 27000)).
634 GFP-Ubiquitin was a kind gift from Nico Dantuma (Addgene plasmid # 11928;
635 RRID:Addgene 11928). For NL2 rescue PALE experiments, the CMV promoter was
636 replaced with GfaABC1D(Lee et al., 2008) for both HA-NL2 (RRID:Addgene_249587) or
637 HA-NL2K749R (RRID:Addgene_249588) via In Fusion Snap Assembly (Takara).

638 pCAG-Cre was a gift from Connie Cepko (Addgene plasmid # 13775 ;
639 http://n2t.net/addgene:13775 ; RRID:Addgene_13775).

640 *CRISPR plasmids:*

641 pX601-mCherry was a gift from Yuet Wai Kan (Addgene plasmid # 84039 ;
642 http://n2t.net/addgene:84039 ; RRID:Addgene_84039). The CMV promoter was
643 replaced with GfaABC1D promoter from the Turbo-BirA plasmids. SaCas9 gRNAs
644 targeting rat *Nlgn2* were designed using CRISPOR(Concordet and Haeussler, 2018)
645 software, and cloned into the BsaI sites in the pX601 vector.

646 - *Nlgn2* gRNA1: AAGAACTGCACGACCGGGCC
647 - *Nlgn2* gRNA2: GTGGTGAACACAGCCTACGG (RRID:Addgene_250933)
648 - *Nlgn2* gRNA3: GCCACACTCAACTACCGTCT (RRID:Addgene_250934)

649 For the CRISPR GFP translation assay, we cloned the NL2 gRNAs and their PAM
650 sequences upstream of and in frame with GFP under the control of the chicken beta
651 actin promoter.

652 **Rat astrocyte and neuron co-culture:**

653 Astrocyte and neuron cultures were performed as described(Baldwin et al., 2021;
654 Stogsdill et al., 2017). Briefly, P1 rat cortices were dissected and digested in ~7.5
655 units/ml Papain (Worthington). A single-cell suspension was extracted by gentle
656 pipetting with ovomucoid solutions (Worthington). Cells were filtered through a 20μm
657 mesh membrane (Elko Filtering 03-20/14) and then split for astrocyte and neuron
658 cultures.

659 For neuronal isolation, cortical cells were applied to negative panning dishes coated
660 with Bandeiraea Simplicifolia Lectin 1 (x2), followed by AffiniPure goat anti-mouse
661 IgG+IgM (H+L) (Jackson ImmunoResearch 115-005-044, RRID: AB_2338451), and
662 AffiniPure goat anti-rat IgG+IgM (H+L) (Jackson ImmunoResearch 112-005-044,
663 RRID:AB_2338094) antibodies to bind unwanted cells and debris. Cell suspensions
664 were passed onto positive panning dishes coated with mouse anti-L1 (ASCS4,
665 Developmental Studies Hybridoma Bank, Univ. Iowa, RRID:AB_528349) to bind cortical
666 neurons (>95% neuron). Adherent cells were collected following several washes with
667 DPBS (Gibco 14287) (supplemented with BSA and insulin) and forceful pipetting with a
668 P1000 pipette. Isolated neurons were pelleted (11 minutes at 200 g) and resuspended
669 in serum-free neuron growth media (NGM; Neurobasal, B27 supplement, 2 mM L-
670 Glutamine, 100 U/mL Pen/Strep, 1 mM NaPyruvate, 4.2 µg/mL Forskolin, 50 ng/mL,
671 BDNF, and 10 ng/mL CNTF). 100,000 neurons were plated onto 12 mm glass
672 coverslips (24-well plate) coated with 10 µg/mL poly-D-lysine (PDL, Sigma P6407) and
673 2 µg/mL laminin, and incubated at 37oC in 10% CO2. On DIV2, neurons were treated
674 with 10µM AraC for one day. Further, on DIV2, media was changed to Neurobasal Plus
675 Growth Media (NGM+; Neurobasal Plus, B27 Plus supplement, 100 U/mL Pen/Strep, 1
676 mM NaPyruvate, 4.2 µg/mL Forskolin, 50 ng/mL, BDNF, and 10 ng/mL CNTF). Neurons
677 were given a 50% media change every third day until astrocyte co-culture. A detailed
678 protocol can be found at: https://www.protocols.io/view/glia-free-cortical-neuron-culture-
679 36wgq3r35lk5/v1.

680 For astrocyte cultures, cortical cells were centrifuged and resuspended in astrocyte
681 growth medium (AGM; DMEM (Gibco 11960), 10% FBS, 10 µM, hydrocortisone, 100

682 U/mL Pen/Strep, 2 mM L-Glutamine, 5 µg/ml Insulin, 1 mM NaPyruvate, 5 µg/ml N-
683 Acetyl-L-cysteine). On the third day in vitro (DIV), astrocytes were washed with DPBS
684 and then shaken vigorously by hand until only adherent astrocytes remained. DPBS
685 was replaced with fresh AGM. AraC was added to the culture at DIV5 for two days. On
686 DIV7, astrocytes were passaged via Trypsin (Gibco) into 6- or 12-well dishes and then
687 transfected on DIV8 with Lipofectamine-LTX. On DIV10, transfected astrocytes were
688 trypsinized and resuspended into NGM+ and plated on neurons at a density of 20,000
689 cells per well (24 well plates). Cells were fixed after 48 hours of co-culture with warm
690 4% PFA (Electron Microscopy Sciences) for exactly 7 minutes.

691 **Immunocytochemistry:**

692 After fixation in 4% warmed PFA for 7 minutes (except in the case of surface staining in
693 which cold PFA was used for 5 minutes), coverslips were blocked in a blocking buffer
694 (150 NaCl, 50 Tris-base, 1% BSA, 100 mM L-lysine, 0.04% Sodium azide, pH 7.4)
695 containing 0.2% Triton X-100 (omitted in surface staining) and 50% NGS was added to
696 the coverslips for 30 minutes, followed by 2 washes of DPBS. Primary antibodies were
697 diluted in a blocking buffer containing 10% NGS and added to the coverslips overnight
698 at 4C. The following antibodies were used: GFAP (1:4000, rabbit, DAKO Z0334,
699 RRID:AB_10013382), GFP (1:1000, chicken, Millipore AB16901, RRID:AB_90890), HA
700 (1:1000, rat, Roche 11867423001, RRID:AB_390918), RFP (1:1000, rabbit, Rockland
701 600-401-379, RRID:AB_2209751). The next day, coverslips were washed 3 times with
702 PBS, and Alexa Fluor conjugated secondaries (Invitrogen: Rb 594, RRID:AB_2534079;
703 Ck 488 RRID:AB_2534096; Rat 594 RRID:AB_10561522) were diluted 1:1000 in
704 blocking buffer containing 10% NGS and incubated for 2 hours at room temperature.

705 After the incubation, the coverslips were washed 3 times and mounted onto glass slides
706 (VWR) with Vectashield mounting media containing DAPI (Vector Laboratories).
707 Imaging was described as before(Stogsdill et al., 2017) on an AxioImager M1 (Zeiss)
708 and a Keyence BZ-X800 at 40X magnification by a blinded investigator. Images were
709 analyzed with Sholl analysis in FIJI (NIH).

710 **CRISPR genome editing efficiency:**

711 To quantify the percent of frameshift inducing mutations, we cloned all 3 NL2 gRNAs
712 and their respective PAM sequences upstream of and in frame with a GFP coding
713 sequence. In HEK293T (ATCC, RRID:CVCL_4V93) cells we co-transfected the pX601-
714 CMV-SaCas9-U6 gRNA plasmids (containing each NL2 gRNA) with the GFP target
715 plasmid. Three days after transfection, the cells were harvested in 1X MPER (Thermo
716 Scientific), incubated at 4C with end-over-end rotation for 10 minutes and then spun at
717 15,000 x g for 5 minutes. The supernatant was kept for downstream western blot
718 analysis. GFP expression on the resulting western blot was quantified using ImageJ and
719 normalized to GAPDH expression. In this assay, a reduction of GFP expression is
720 interpreted to be genomic cutting by the corresponding gRNA.

721 **In vitro Sholl Analysis:**

722 Sholl Analysis was performed in FIJI (NIH, v1.53c) using the Sholl Analysis plug-in
723 (v4.0.1). The number of intersections is measured with concentric circles at every 1μm
724 starting from a radius of 10μm from the center of the nucleus. Resulting values were
725 then analyzed in R (v4.0.0 and above) using an in-home pipeline which can be found
726 here: https://github.com/Eroglu-Lab/In-Vitro-Sholl. The final graphs are the average of

727 each biological replicate, not of each image. The line graphs were generated using the
728 LOESS method (ggplot2 [Hadley Wickham], stat_smooth function) and the variance
729 (standard error) is represented with the colored lines.

730 **Postnatal astrocyte labeling by electroporation (PALE):**

731 PALE was performed as previously described(Baldwin et al., 2021). Briefly, P0-P1 pups
732 were placed on a glove on ice for < 5 minutes until unresponsive. 1-2µg (in 1-2µl total
733 volume) of plasmid was loaded into a pulled glass pipette containing 1% fast green dye
734 (Sigma F7252). The glass pipette was then inserted into one lateral ventricle of the
735 mouse brain and DNA was injected. Electrodes were then positioned above the visual
736 cortex (positive end) and below the jaw (negative end) and five 50ms pulses of 100V
737 with an interpulse interval of 950ms were applied. Pups recovered on a heating pad and
738 were then returned to the home cage with the dam. Each litter received a random
739 assignment of experimental groups. All animals that recovered after surgery with no
740 visible health issues were kept for the analysis. Animals were transcardially perfused
741 with 4% PFA at P21.

742 **Immunohistochemistry:**

743 Mice were perfused transcardially with 4% PFA and were transferred to 4% PFA
744 overnight before incubation with 30% sucrose in TBS. Coronal sections were collected
745 on a cryostat (Leica) at either 40µm (iBioID, synaptic staining) or 100µm (territory
746 volume and 3D Sholl). Sections were washed 3 times for 10 minutes on a shaker in
747 0.2%(40µm sections) or 0.4%(100µm sections) Triton-X in TBS (TBST). Sections were
748 blocked in 10% Goat serum in TBST for 1 hour on the shaker at room temperature.

749 Primary antibodies: PSD95 (1:300, rabbit, Invitrogen 51-6900, RRID:AB_2533914),
750 Gephyrin (1:500, mouse, Synaptic Systems 147011, RRID:AB_2810215), RFP (1:1000,
751 chicken, Rockland 600-901-379, RRID:AB_10704808, used for synaptic staining),
752 Bassoon (1:500, guinea pig, Synaptic Systems 141318, RRID:AB_2927388), HA
753 (1:200, rat, Roche 11867423001, RRID:AB_390918), RFP [for detecting mCherry CAAX
754 in shRNA PALE experiments] (1:1000, rabbit, Rockland 600-401-379,
755 RRID:AB_2209751), RFP nanobody 568 coupled [for detecting tdTomato in Ai14 mice
756 for NL2 rescue PALE experiments] (1:100, Synaptic Systems,N0404-AF568-L,
757 RRID:AB_2209751), Sox9 (1:1000, Rabbit, Millipore AB5535, RRID:AB_2239761),
758 NeuN (1:1000, Mouse, Millipore MAB377, RRID:AB_2298772) were diluted in fresh
759 blocking buffer and incubated either overnight (40µm) or for 3 nights (100µm). Alexa
760 Fluor or Streptavidin conjugated fluorescent secondaries (Invitrogen: Rabbit 405+
761 RRID:AB_2890548; Mouse IgG1 488 RRID:AB_2535764, Chicken 568
762 RRID:AB_2534098, Guinea Pig 647 RRID:AB_2535867, Rat 488 RRID:AB_2534074,
763 Rabbit 594 RRID:AB_2534095, Streptavidin Alexa Fluor conjugate (Thermo Fisher,
764 S32357)) were diluted in blocking buffer at 1:200 and incubated on tissue for 3 hours at
765 room temperature. DAPI was added in the final wash before mounting. Sections were
766 mounted on glass slides with mounting media (90% Glycerol, 20 mM Tris pH 8.0, 0.5%
767 n-Propyl gallate).

768 **Synapse quantification:**

769 Images for synapse quantification were acquired on an Olympus FV 3000 at 60X
770 magnification with 1.64X zoom, in 1µm stacks with a 0.34µm step size. We used
771 SynBot(Savage et al., 2024) (https://github.com/Eroglu-Lab/Syn_Bot) in FIJI to quantify

772 the colocalization of Bassoon and Psd95 (excitatory) or Bassoon and Gepyhrin
773 (inhibitory) synapses for the entire image using manual thresholding. Using a custom
774 macro in FIJI (https://github.com/Eroglu-Lab/Sakers-et-al-2025), we then cropped the
775 binarized synaptic output images to draw an ROI around the labeled astrocyte and
776 quantify the number of synaptic puncta within and outside the ROI. These synaptic
777 puncta were normalized to the corresponding ROI to obtain a synapse density. The data
778 were analyzed with a linear mixed effects ANOVA in R.

779 **Imaris territory volume and 3D Sholl analysis:**

780 100μm sections were imaged on an Olympus FV 3000 at 60X magnification, with 2X
781 zoom. Single astrocytes were captured in a frame in a Z stack at 0.5μm step size to
782 capture the whole astrocyte. Imaris v9.9 (Bitplane) was used to reconstruct images
783 using the filament tracer in 3D. We used two custom extensions to quantify filament
784 complexity (3D Sholl analysis) every 5μm from the cell nucleus [note that this is different
785 from 2D Sholl analysis where a measurement is taken every 1μm from the cell nucleus].
786 A linear mixed model followed by Dunnett's post-hoc test was used to analyze the 3D
787 Sholl data using a custom R script found at: https://github.com/Eroglu-Lab/In-vivo-Sholl-
788 Analysis. The whole astrocyte territory volume was calculated using the Convex Hull
789 function in Imaris on the cell surface territory. Analysis of territory volume was analyzed
790 in R using a one-way repeated measures ANOVA to account for multiple images taken
791 per animal, followed by Dunnett's post-hoc test.

792 **Adeno-associated virus production:**

793 Purified AAV was produced as described previously(Baldwin et al., 2021). Briefly,
794 HEK293T cells were transfected with pAd-DELTA F6, serotype plasmid AAV PHP.eB,
795 and AAV plasmids (pZac2.1 Turbo ID constructs). Three days after transfection, cells
796 were collected in 15 mM NaCl, 5 mM Tris-HCl, pH 8.5, and lysed with repeat freeze-
797 thaw cycles followed by treatment with Benzonase (Novagen 70664) at 37°C for 30
798 minutes. Lysed cells were pelleted by centrifugation and the supernatant, containing
799 AAV was applied to an Optiprep density gradient (Sigma D1556, 15%, 25%, 40%, and
800 60%) and centrifuged at 67,000 rpm using a Beckman Ti-70 rotor for 1 hour. The AAV-
801 enriched fraction was isolated from between 40% and 60% iodixanol solution and
802 concentrated by repeated washes with sterile PBS in an Amicon Ultra-15 filtration unit
803 (NMWL: 100 kDa, Millipore UFC910008) to a final volume of ~100 µL and aliquoted for
804 storage at −80°C.

805 **In vivo BioID:**

806 Pregnant CD1 dams were ordered from Charles River Laboratories. On P1, pups were
807 anesthetized by hypothermia and subsequently injected intracranially at a depth of 2mm
808 with 1µl equal viral titers of either NL2-Turbo-BirA or Turbo-BirA as previously
809 described. Mice were treated with 0.75mL of 5mM Biotin in sterile PBS via
810 subcutaneous injections once a day from P18 to P20. On P21, mice were sacrificed with
811 200 mg/kg tribromoethanol (avertin) and transcardially perfused with TBS/Heparin for 5
812 minutes to wash out excess biotin. Subsequently, cortices were rapidly dissected in
813 DPBS and flash-frozen in liquid nitrogen.

814 All solutions were made fresh using proteomics-grade chemicals and solvents. Brains
815 were homogenized with approximately 12 strokes in a glass homogenizer and Teflon

816 pestle in 1mL Lysis buffer [50mM Tris/HCl pH7.5, 150mM NaCl, 1mM EDTA with
817 protease inhibitors (Roche)] on ice. An equal volume of 2X RIPA [50mM Tris/HCl pH7.5,
818 150mM NaCl, 1mM EDTA, 0.4% SDS, 2%TritonX100, 2% deoxycholate] was added to
819 the lysates. Lysates were then sonicated (level 9) for 30 seconds (3 x 10s) total,
820 followed by centrifugation at 15,000 RPM for 10 minutes at 4C. The supernatant was
821 transferred to an ultracentrifuge 1.5mL tube (Beckman Coulter) and spun in a TLA-55
822 rotor (Beckman coulter) in an ultracentrifuge at 40,000 RPM for 30 minutes at 4C.
823 Supernatants were transferred to a low-protein binding tube (Eppendorf) and SDS was
824 added to a final concentration of 1%. Samples were then briefly vortexed and heated at
825 45C for 45 mins, cooled on ice, and spun at 15,000RPM for 30 minutes at 4C. 70 µl
826 Neutravidin beads (ThermoFisher 29202) were prepared per condition by washing with
827 1mL of 2X RIPA two times. The samples were transferred to 15mL tubes (1 brain per
828 IP, 3 brains per condition), and washed Neutravidin beads were added to the sample
829 supernatant. 30ul of the supernatant was saved for western blot analysis. The beads
830 and samples were incubated overnight at 4C with rotation. The next day beads were
831 sequentially washed with 1mL of the following solutions for 10 minutes with rotation,
832 followed by two-minute spins: 2% SDS x2, Wash buffer (1% TritonX100, 1%
833 deoxycholate, 25 mM LiCl) x2, 1M NaCl x2, 50mM Ammonium bicarbonate x5. Elution
834 buffer was prepared during the last washes by adding 1.2mg of biotin to 2X sample
835 buffer [4% SDS, 20% glycerol, 0.1% beta-mercaptoethanol, 125mM Tris pH 6.8 to 20mL
836 with keratin-free water]. 70ul of elution buffer was added to the beads and samples
837 were then heated at 60C for 15 minutes to elute bound proteins. The sample was stored
838 at -80C before mass spec analysis, and 5ul of the eluate was saved for western blotting.

839 All washes and elution were done in a tissue culture hood, in sterile conditions to avoid
840 keratin contamination.

841 **Mass spectrometry:**

842 Sample Preparation: The Duke Proteomics Core Facility (DPCF) received 6 samples (3
843 replicates each of two conditions). Samples were reduced with 10 mM dithiothreitol for
844 30 min at 80C and alkylated with 20 mM iodoacetamide for 30 min at room temperature.
845 Next, they were supplemented with a final concentration of 1.2% phosphoric acid and
846 597 µL of S-Trap (Protifi) binding buffer (90% MeOH/100mM TEAB). Proteins were
847 trapped on the S-Trap, digested using 20 ng/µl sequencing grade trypsin (Promega) for
848 1 hr at 47C, and eluted using 50 mM TEAB, followed by 0.2% FA, and lastly using 50%
849 ACN/0.2% FA. All samples were then lyophilized to dryness and resuspended in 12µL
850 1%TFA/2% acetonitrile containing 12.5 fmol/µL yeast alcohol dehydrogenase
851 (ADH_YEAST). A QC Pool was created from 3uL of each sample. All QC Pools were
852 run periodically throughout the acquisition period.

853 Quantitative Analysis, Methods: Quantitative LC/MS/MS was performed on 3 µL of each
854 sample, using a nanoAcquity UPLC system (Waters Corp) coupled to a Thermo
855 Orbitrap Fusion Lumos high-resolution accurate mass tandem mass spectrometer
856 (Thermo) via a nanoelectrospray ionization source. Briefly, the sample was first trapped
857 on a Symmetry C18 20 mm × 180 µm trapping column (5 µl/min at 99.9/0.1 v/v
858 water/acetonitrile), after which the analytical separation was performed using a 1.8 µm
859 Acquity HSS T3 C18 75 µm × 250 mm column (Waters Corp.) with a 90-min linear
860 gradient of 5 to 30% acetonitrile with 0.1% formic acid at a flow rate of 400
861 nanoliters/minute (nL/min) with a column temperature of 55C. Data collection on the

862 Fusion Lumos mass spectrometer was performed in a data-dependent acquisition
863 (DDA) mode of acquisition with a r=120,000 (@ m/z 200) full MS scan from m/z 375 –
864 1500 with a target AGC value of 2e5 ions. MS/MS scans were acquired at a Rapid scan
865 rate (Ion Trap) with an AGC target of 5e3 ions and a max injection time of 100 ms. The
866 total cycle time for MS and MS/MS scans was 2 sec. A 20s dynamic exclusion was
867 employed to increase the depth of coverage. The total analysis cycle time for each
868 sample injection was approximately 2 hours. Following 9 total UPLC-MS/MS analyses
869 (excluding conditioning runs, but including 3 replicate QC Pool), data was imported into
870 Proteome Discoverer 2.3 (Thermo Scientific Inc.), and analyses were aligned based on
871 the accurate mass and retention time of detected ions ("features") using Minora Feature
872 Detector algorithm in Proteome Discoverer. Relative peptide abundance was calculated
873 based on the area-under-the-curve (AUC) of the selected ion chromatograms of the
874 aligned features across all runs. The MS/MS data was searched against the SwissProt
875 M. musculus database (downloaded in Apr2017) and an equal number of reversed-
876 sequence "decoys" for false discovery rate determination. Mascot Distiller and Mascot
877 Server (v 2.5, Matrix Sciences) were utilized to produce fragment ion spectra and to
878 perform the database searches. Database search parameters included fixed
879 modifications on Cys (carbamidomethyl) and variable modifications on Meth (oxidation)
880 and Asn and Gln (deamidation). Peptide Validator and Protein FDR Validator nodes in
881 Proteome Discoverer were used to annotate the data at a maximum 1% protein false
882 discovery rate.

883 *Statistical analysis of iBioID data:*

884 In vivo BioID has an inherently high background in mass spectrometry due to the time
885 necessary for biotin to accumulate in the system, and the diffuse nature of AMP-biotin.
886 We controlled for this background using a soluble (non-bait) TurboID enzyme in both
887 astrocytes and neurons, as this would accurately replicate the high background in bait
888 conditions. Further, to account for differences in expression due to the size differenced
889 of soluble TurboID and NL-tagged TurboID, we employed a robust-mean normalization
890 which excludes the top and bottom 10% of signal intensities and mitigates the
891 influences of outliers. The BioID datasets were generated from distinct viral constructs
892 and cellular contexts, thus necessitating an enrichment-over-control design. To do so,
893 we calculated the fold changes and used a two-tailed heteroscedastic t-test on log2-
894 transformed data comparing the NL2 and Turbo BioID groups, and performed FDR
895 correction to obtain high-confidence putative interactors.

896 **Western blotting:**

897 iBioID: 5ul of IP eluate and 30ul of sonicated lysate were run on a 4-15% Mini-Protean
898 precast gel (BioRad). After transfer, membranes were blocked in Odyssey blocking
899 buffer (LI-COR) diluted in PBS (1:1) followed by incubation in the same buffer with
900 Alexa 680 conjugated streptavidin (Invitrogen). Membranes were imaged on a LI-COR
901 Odyssey CLx.

902 All other blots: Equal protein (measured by Bicinchoninic Acid Protein Assay (BCA,
903 Pierce)) was loaded on a 4-15% Mini-Protean precast gel (BioRad). In the case of
904 immunoprecipitations, input samples were loaded as an equal percentage of total
905 sample homogenate, and the entirety of the IP eluate was run per lane. Gels were
906 transferred using a Power Blotter System (Invitrogen) and then blocked in a Blocking

907 Buffer for Fluorescent Western Blotting (Rockland, MB-070) diluting in PBS (1:1). The
908 following primary antibodies were used for blotting: Rabbit anti-Nedd4l (Cell Signaling
909 Technology, 4013S, 1:1000, RRID:AB_1904063), Rabbit anti-V5 (Cell Signaling
910 Technology, 13202S, 1:500, RRID:AB_2687461), Chicken anti-HA (Aves Labs, ET-
911 HA100, 1:2000, RRID:AB_2313511), Rabbit anti-GFP (Novus Biologicals, NB600-308,
912 1:1000, RRID:AB_10003058), Mouse anti-Gapdh (Abcam, ab8245, 1:2500,
913 RRID:AB_2107448), Mouse anti-Actin (Sigma-Aldrich, A5441, 1:2000,
914 RRID:AB_476744) diluted in blocking buffer. LI-COR 680 or 800 fluorescent secondary
915 antibodies (Chicken 800 RRID:AB_10974977; Rabbit 800 RRID:AB_621848; Mouse
916 800 RRID:AB_621842, Rabbit 680 RRID:AB_621845, Chicken 680 RRID:AB_1850018)
917 were diluted 1:2500 in blocking buffer and blots were imaged on a LI-COR Odyssey
918 CLx.

919 **Lentivirus production and transduction:**

920 8-10 million 293T cells were plated in a T-75 culture flask and transfected using
921 Xtremegene HP Transfection Reagent (Roche, 06366236001) with the following
922 plasmids: pLKO.1 puromycin-resistant shRNA plasmids (described above), VSVG (an
923 envelope plasmid), and dR8.91 packaging plasmid. One day post-transfection, the
924 media was replaced with astrocyte growth media, and lentivirus was collected on days 2
925 and 3 and filtered through a 40μm syringe filter. Media was tested for lentiviral particles
926 using Lenti-X Go Stix (Takara, 631280). Astrocytes were treated with 500μl of lentiviral
927 media supernatant, and 1μg/mL polybrene on DIV8. On DIV10, astrocytes were treated
928 with 1μg/mL puromycin every other day until a non-transduced well was completely
929 dead. Cells were lysed for qPCR as described below. Cells collected for western blot

930 were collected in T-PER (Thermo Scientific, 78510) and protein was measured using a
931 BCA protein assay (Thermo Scientific, 23227).

932 **Gene ontology analysis:**

933 Gene ontology analysis was performed in R using the package clusterProfiler v4.6.2(Wu
934 et al., 2021). Proteins from iBioID lists that were at least 1.5 fold enriched at a p-value of
935 <0.05, compared to respective controls described in legends, were subjected to
936 Biological Processes enrichment. Resulting output was reduced using the simplify
937 function in clusterProfiler. The top 5-10 categories (sorted by adjusted p-value) were
938 plotted in R. The entire enrichment can be found in Supplemental Dataset 2.

939 **Immunoprecipitation:**

940 4 million 293T cells (ATCC, RRID:CVCL_4V93) (passage #8-15) were plated in 10cm
941 dishes and then transfected the next day with 2.5µg of each plasmid using the
942 Xtremegene HP Transfection Reagent (Roche, 06366236001) according to the
943 manufacturer's protocol. 48 hours post transfection cells were washed with 1X TBS
944 supplemented with calcium and magnesium and pelleted. Cell pellets were
945 resuspended in 400µl of lysis buffer (25mM Tris pH 7.4, 1mM Calcium Chloride, 1mM
946 Magnesium Chloride, 150mM Sodium Chloride, 0.5% NP-40, 1X EDTA-free protease
947 inhibitor cocktail (Roche)) and centrifuged at 20,000xg for 10 minutes. 5% of the
948 supernatant was saved for input samples, and the remaining lysate was diluted with
949 lysis buffer without NP-40 for IP. Lysate was added to 30µl of magnetic anti-HA beads
950 (Pierce, 88836) overnight at 4C with rotation. Beads were collected on a magnetic rack
951 and washed 3 times with wash buffer (25mM Tris pH 7.4, 1mM Calcium Chloride, 1mM

952 Magnesium Chloride, 150mM Sodium Chloride, 0.1% NP-40, 1X EDTA-free protease
953 inhibitor cocktail (Roche)). Beads were eluted with 2X Laemmli buffer (Bio-Rad,
954 1610737) at 42C for 15 minutes and then denatured with 5% β-mercaptoethanol at 45C
955 for 45 minutes before loading on SDS-PAGE.

956 **Ubiquitination assay:**

957 293T cells were transfected as indicated in the immunoprecipitation subsection. 48
958 hours post-transfection, cells were treated with 25μM MG-132 (Sigma-Aldrich, 474790)
959 for 2-4 hours to block the proteasome. Cells were washed 3 times in ice-cold 1X TBS
960 supplemented with magnesium, calcium, and N-ethylmaleimide (NEM) (Sigma-Aldrich,
961 E3876) to block deubiquitinases and then pelleted. Cells were resuspended in 1X RIPA
962 buffer with SDS (50 mM Tris-HCl pH 7.4, 150 mM NaCl, 1% NP-40, 0.5% Sodium
963 Deoxycholate, 1% Sodium dodecyl sulfate, supplemented with 1X protease inhibitor and
964 20mM NEM) and then boiled for 5 minutes to disrupt protein-protein interactions. The
965 lysates were diluted 10X with 1X RIPA without SDS and incubated on a rotator at 4C for
966 1 hour. The lysates were then pelleted at 15,000xg for 15 minutes and the supernatant
967 was added to magnetic anti-HA beads, and 5% of the supernatant was collected for
968 input fraction. Elution was performed identically to the immunoprecipitation subsection
969 above. For ubiquitination assay in primary rat astrocytes, 5 million DIV7 astrocytes
970 (prepared as described above) were nucleofected with the Basic Glial Cells
971 Nucleofection Kit (Lonza) and 5ug of each plasmid. 24 hours after nucleofection, the
972 media was changed to remove dead cells and nucleofection solution. Ubiquitination IP
973 was performed 3 days after nucleofection in the same manner as 293T cells.

974 **Degradation assay:**

975 350,000 HEK 293T cells were plated into wells of a 6-well plate and then transfected
976 one day later with 1µg of each plasmid via Xtremegene HP Transfection Reagent
977 reagent (Roche #06366236001). 48 hours later cells were treated with cycloheximide
978 (100µg/mL). At each time point, the collected cells were washed with 1X TBS with
979 magnesium and calcium, pelleted, and then resuspended in 1X RIPA (Sigma-Aldrich)
980 supplemented with protease inhibitors. Lysates were incubated at 4C with rotation for
981 40 minutes, centrifuged at 20,000xg at 4C and supernatants were saved for protein
982 quantitation via BCA. 5µg of total protein was loaded on a 4-15% SDS-PAGE. Three
983 independent cultures were used for statistical analysis.

984 **Statistics:**

985 Experiments were randomized where applicable and analyses were run by an
986 experimenter blind to the condition. All in vitro experiments were performed at least 3
987 times (3 different cultures), with 20+ cells imaged per replicate. Note that some
988 conditions were plotted across several figures (i.e. shNL2 in Figure S1, Figure 1; shNL2
989 + HA-NL2 Figure 1D and F and S1, and shNL2 in Figure 5), as experiments were done
990 in parallel. All analyses were done in R (v4.0.0 and above). An R script with
991 reproducible data can be found at the following links for both in vitro analysis
992 (https://github.com/Eroglu-Lab/In-Vitro-Sholl) and in vivo analysis
993 (https://github.com/Eroglu-Lab/In-vivo-Sholl-Analysis). Statistical analyses were
994 performed using N of independent culture or animal rather than image to avoid
995 pseudoreplication artifacts. Specific details on sample size, and test applied can be
996 found in the figure legends and Methods subsections and in Table S1.

997

998 **Data availability statement**

999 The mass spectrometry proteomics data have been deposited to the ProteomeXchange
1000 Consortium via the PRIDE(Perez-Riverol et al., 2022) partner repository with the
1001 dataset identifier PXD049185. All data in this manuscript can be found in the attached
1002 Source Data file.

1003 **Acknowledgments**

1004 This work was supported by the National Institutes of Health (R01 NS102237 and R01
1005 DA047258 to C. Eroglu, F32 NS112565 for K. Sakers, and F31NS125985 for J.J.
1006 Ramirez), and fellowships from The Ruth K. Broad Biomedical Research Foundation at
1007 Duke (to N. Elazar) and the Life Sciences Research Foundation (to N. Elazar).

1008 We thank Dr. Roger Nicoll for the NL chimeric constructs. We thank members of Dr.
1009 Scott Soderling's lab for iBioID constructs and protocols. We thank Dr. Dolores Irala for
1010 her help with figure organization and design. We thank Dr. Jessica Moore, Dr. Dolores
1011 Irala, Dr. Jeff Stogsdill and Dr. Debra Silver for the critical review of this manuscript.

1012 C. Eroglu is an HHMI Investigator. This article is subject to HHMI's Open Access to
1013 Publications policy. Under this policy, the accepted research article will be published
1014 under a Creative Commons Attribution 4.0 International (CC BY4.0). Therefore, this
1015 article will be freely available to the public by the publication date.

1016 The authors declare no competing financial interests.

1017 **Author contributions**

Conceptualization: K. Sakers and C. Eroglu; Investigation: K. Sakers, J.J. Ramirez, N. Elazar, L. Nagendren; Methodology: K. Sakers, C. Eroglu; Data curation: K. Sakers; Formal analysis: K. Sakers, E. Soderblom; Writing: K. Sakers, C. Eroglu. Project administration: K. Sakers; Supervision: C. Eroglu; Funding acquisition: C. Eroglu, K. Sakers, N. Elazar and J.J. Ramirez

1023 **REFERENCES**

1024 Ackerman, S.D., N.A. Perez-Catalan, M.R. Freeman, and C.Q. Doe. 2021. Astrocytes close a motor circuit
1025 critical period. *Nature*. 592:414–420. doi:10.1038/s41586-021-03441-2.

1026 Altas, B., H.-J. Rhee, A. Ju, H.C. Solís, S. Karaca, J. Winchenbach, O. Kaplan-Arabaci, M. Schwark, M.C.
1027 Ambrozkiewicz, C. Lee, L. Spieth, G.L. Wieser, V.K. Chaugule, I. Majoul, M.A. Hassan, R. Goel,
1028 S.M. Wojcik, N. Koganezawa, K. Hanamura, D. Rotin, A. Pichler, M. Mitkovski, L. de Hoz, A.
1029 Poulopoulos, H. Urlaub, O. Jahn, G. Saher, N. Brose, J. Rhee, and H. Kawabe. 2024. Nedd4-2-
1030 dependent regulation of astrocytic Kir4.1 and Connexin43 controls neuronal network activity. *J.*
1031 *Cell Biol.* 223:e201902050. doi:10.1083/jcb.201902050.

1032 Babaev, O., P. Botta, E. Meyer, C. Müller, H. Ehrenreich, N. Brose, A. Lüthi, and D. Krueger-Burg. 2016.
1033 Neuroligin 2 deletion alters inhibitory synapse function and anxiety-associated neuronal
1034 activation in the amygdala. *Neuropharmacology*. 100:56–65.
1035 doi:10.1016/j.neuropharm.2015.06.016.

1036 Baldwin, K.T., K.K. Murai, and B.S. Khakh. 2023. Astrocyte morphology. *Trends Cell Biol.* S0962-
1037 8924(23)00204–0. doi:10.1016/j.tcb.2023.09.006.

1038 Baldwin, K.T., C.X. Tan, S.T. Strader, C. Jiang, J.T. Savage, X. Elorza-Vidal, X. Contreras, T. Rülicke, S.
1039 Hippenmeyer, R. Estévez, R.-R. Ji, and C. Eroglu. 2021. HepaCAM controls astrocyte self-
1040 organization and coupling. *Neuron*. 109:2427-2442.e10. doi:10.1016/j.neuron.2021.05.025.

1041 Barrow, S.L., J.R. Constable, E. Clark, F. El-Sabeawy, A.K. McAllister, and P. Washbourne. 2009.
1042 Neuroligin1: a cell adhesion molecule that recruits PSD-95 and NMDA receptors by distinct
1043 mechanisms during synaptogenesis. *Neural Develop.* 4:17. doi:10.1186/1749-8104-4-17.

1044 Binda, C.S., Y. Nakamura, J.M. Henley, and K.A. Wilkinson. 2019. Sorting nexin 27 rescues neuroligin 2
1045 from lysosomal degradation to control inhibitory synapse number. *Biochem. J.* 476:293–306.
1046 doi:10.1042/BCJ20180504.

1047 Boisvert, M.M., G.A. Erikson, M.N. Shokhirev, and N.J. Allen. 2018. The Aging Astrocyte Transcriptome
1048 from Multiple Regions of the Mouse Brain. *Cell Rep.* 22:269–285.
1049 doi:10.1016/j.celrep.2017.12.039.

1050 Booth, H.D.E., W.D. Hirst, and R. Wade-Martins. 2017. The Role of Astrocyte Dysfunction in Parkinson's
1051 Disease Pathogenesis. *Trends Neurosci.* 40:358–370. doi:10.1016/j.tins.2017.04.001.

1052 Branon, T.C., J.A. Bosch, A.D. Sanchez, N.D. Udeshi, T. Svinkina, S.A. Carr, J.L. Feldman, N. Perrimon, and
1053 A.Y. Ting. 2018. Efficient proximity labeling in living cells and organisms with TurboID. *Nat.*
1054 *Biotechnol.* 36:880–887. doi:10.1038/nbt.4201.

1055 Bruce, M.C., V. Kanelis, F. Fouladkou, A. Debonneville, O. Staub, and D. Rotin. 2008. Regulation of
1056 Nedd4-2 self-ubiquitination and stability by a PY motif located within its HECT-domain. *Biochem.*
1057 *J.* 415:155–163. doi:10.1042/BJ20071708.

1058 Bushong, E.A., M.E. Martone, and M.H. Ellisman. 2004. Maturation of astrocyte morphology and the
1059 establishment of astrocyte domains during postnatal hippocampal development. *Int. J. Dev.*
1060 *Neurosci.* 22:73–86. doi:10.1016/j.ijdevneu.2003.12.008.

1061 Bushong, E.A., M.E. Martone, Y.Z. Jones, and M.H. Ellisman. 2002. Protoplasmic astrocytes in CA1
1062 stratum radiatum occupy separate anatomical domains. *J. Neurosci. Off. J. Soc. Neurosci.*
1063 22:183–192. doi:10.1523/JNEUROSCI.22-01-00183.2002.

1064 Chanda, S., W.D. Hale, B. Zhang, M. Wernig, and T.C. Südhof. 2017. Unique versus Redundant Functions
1065 of Neuroligin Genes in Shaping Excitatory and Inhibitory Synapse Properties. *J. Neurosci. Off. J.*
1066 *Soc. Neurosci.* 37:6816–6836. doi:10.1523/JNEUROSCI.0125-17.2017.

1067 Chen, H.I., A. Einbond, S.J. Kwak, H. Linn, E. Koepf, S. Peterson, J.W. Kelly, and M. Sudol. 1997.
1068 Characterization of the WW domain of human yes-associated protein and its polyproline-
1069 containing ligands. *J. Biol. Chem.* 272:17070–17077. doi:10.1074/jbc.272.27.17070.

1070 Chih, B., H. Engelman, and P. Scheiffele. 2005. Control of excitatory and inhibitory synapse formation by
1071 neuroligins. *Science*. 307:1324–1328. doi:10.1126/science.1107470.

1072 Chih, B., L. Gollan, and P. Scheiffele. 2006. Alternative splicing controls selective trans-synaptic
1073 interactions of the neuroligin-neurexin complex. *Neuron*. 51:171–178.
1074 doi:10.1016/j.neuron.2006.06.005.

1075 Clarke, L.E., S.A. Liddelow, C. Chakraborty, A.E. Münch, M. Heiman, and B.A. Barres. 2018. Normal aging
1076 induces A1-like astrocyte reactivity. *Proc. Natl. Acad. Sci.* 115:E1896–E1905.
1077 doi:10.1073/pnas.1800165115.

1078 Concordet, J.-P., and M. Haeussler. 2018. CRISPOR: intuitive guide selection for CRISPR/Cas9 genome
1079 editing experiments and screens. *Nucleic Acids Res.* 46:W242–W245. doi:10.1093/nar/gky354.

1080 Endo, F., A. Kasai, J.S. Soto, X. Yu, Z. Qu, H. Hashimoto, V. Gradinaru, R. Kawaguchi, and B.S. Khakh. 2022.
1081 Molecular basis of astrocyte diversity and morphology across the CNS in health and disease.
1082 *Science*. 378:eadc9020. doi:10.1126/science.adc9020.

1083 Farhy-Tselnicker, I., M.M. Boisvert, H. Liu, C. Dowling, G.A. Erikson, E. Blanco-Suarez, C. Farhy, M.N.
1084 Shokhirev, J.R. Ecker, and N.J. Allen. 2021. Activity-dependent modulation of synapse-regulating
1085 genes in astrocytes. *eLife*. 10:e70514. doi:10.7554/eLife.70514.

1086 Farizatto, K.L.G., and K.T. Baldwin. 2023. Astrocyte-synapse interactions during brain development. *Curr.*
1087 *Opin. Neurobiol.* 80:102704. doi:10.1016/j.conb.2023.102704.

1088 Giannone, G., M. Mondin, D. Grillo-Bosch, B. Tessier, E. Saint-Michel, K. Czöndör, M. Sainlos, D. Choquet,
1089 and O. Thoumine. 2013. Neurexin-1β Binding to Neuroligin-1 Triggers the Preferential
1090 Recruitment of PSD-95 versus Gephyrin through Tyrosine Phosphorylation of Neuroligin-1. *Cell*
1091 *Rep.* 3:1996–2007. doi:10.1016/j.celrep.2013.05.013.

1092 Goel, K., and J.E. Ploski. 2022. RISC-y Business: Limitations of Short Hairpin RNA-Mediated Gene
1093 Silencing in the Brain and a Discussion of CRISPR/Cas-Based Alternatives. *Front. Mol. Neurosci.*
1094 15. doi:10.3389/fnmol.2022.914430.

1095 Golf, S.R., J.H. Trotter, J. Wang, G. Nakahara, X. Han, M. Wernig, and T.C. Südhof. 2025. Deletion of
1096 Neuroligins from Astrocytes Does Not Detectably Alter Synapse Numbers or Astrocyte
1097 Cytoarchitecture by Maturity. *eLife*. 12. doi:10.7554/eLife.87589.3.

1098 Gupta, S., J.A. Stamatoyannopoulos, T.L. Bailey, and W.S. Noble. 2007. Quantifying similarity between
1099 motifs. *Genome Biol.* 8:R24. doi:10.1186/gb-2007-8-2-r24.

1100 Gutmann, D.H., A. Loehr, Y. Zhang, J. Kim, M. Henkemeyer, and A. Cashen. 1999. Haploinsufficiency for
1101 the neurofibromatosis 1 (NF1) tumor suppressor results in increased astrocyte proliferation.
1102 *Oncogene*. 18:4450–4459. doi:10.1038/sj.onc.1202829.

1103 Halff, E.F., B.R. Szulc, F. Lesept, and J.T. Kittler. 2019. SNX27-Mediated Recycling of Neuroligin-2
1104 Regulates Inhibitory Signaling. *Cell Rep.* 29:2599-2607.e6. doi:10.1016/j.celrep.2019.10.096.

1105 Hatstat, A.K., M.D. Pupi, and D.G. McCafferty. 2021. Predicting PY motif-mediated protein-protein
1106 interactions in the Nedd4 family of ubiquitin ligases. *PLOS ONE*. 16:e0258315.
1107 doi:10.1371/journal.pone.0258315.

1108 Holt, L.M., R.D. Hernandez, N.L. Pacheco, B. Torres Ceja, M. Hossain, and M.L. Olsen. 2019. Astrocyte
1109 morphogenesis is dependent on BDNF signaling via astrocytic TrkB.T1. *eLife*. 8:e44667.
1110 doi:10.7554/eLife.44667.

1111 Hunker, A.C., and L.S. Zweifel. 2020. Protocol to Design, Clone, and Validate sgRNAs for *In Vivo* Reverse
1112 Genetic Studies. *STAR Protoc.* 1:100070. doi:10.1016/j.xpro.2020.100070.

1113 Ilsley, J.L., M. Sudol, and S.J. Winder. 2002. The WW domain: linking cell signalling to the membrane
1114 cytoskeleton. *Cell. Signal.* 14:183–189.

1115 Irie, M., Y. Hata, M. Takeuchi, K. Ichtchenko, A. Toyoda, K. Hirao, Y. Takai, T.W. Rosahl, and T.C. Südhof.
1116 1997. Binding of Neuroligins to PSD-95. *Science*. 277:1511–1515.
1117 doi:10.1126/science.277.5331.1511.

1118 Jamain, S., H. Quach, C. Betancur, M. Råstam, C. Colineaux, I.C. Gillberg, H. Söderström, B. Giros, M.
1119 Leboyer, C. Gillberg, and T. Bourgeron. 2003. Mutations of the X-linked genes encoding
1120 neuroligins NLGN3 and NLGN4 are associated with autism. *Nat. Genet.* 34:27–29.
1121 doi:10.1038/ng1136.

1122 Kang, Y., Y. Ge, R.M. Cassidy, V. Lam, L. Luo, K.-M. Moon, R. Lewis, R.S. Molday, R.O.L. Wong, L.J. Foster,
1123 and A.M. Craig. 2014. A Combined Transgenic Proteomic Analysis and Regulated Trafficking of
1124 Neuroligin-2. *J. Biol. Chem.* 289:29350–29364. doi:10.1074/jbc.M114.549279.

1125 Kasanov, J., G. Pirozzi, A.J. Uveges, and B.K. Kay. 2001. Characterizing Class I WW domains defines key
1126 specificity determinants and generates mutant domains with novel specificities. *Chem. Biol.*
1127 8:231–241.

1128 Kato, Y., M. Ito, K. Kawai, K. Nagata, and M. Tanokura. 2002. Determinants of Ligand Specificity in
1129 Groups I and IV WW Domains as Studied by Surface Plasmon Resonance and Model Building *. *J.*
1130 *Biol. Chem.* 277:10173–10177. doi:10.1074/jbc.M110490200.

1131 Kato, Y., K. Nagata, M. Takahashi, L. Lian, J.J. Herrero, M. Sudol, and M. Tanokura. 2004. Common
1132 mechanism of ligand recognition by group II/III WW domains: redefining their functional
1133 classification. *J. Biol. Chem.* 279:31833–31841. doi:10.1074/jbc.M404719200.

1134 Kirkeby, S., D. Moe, T.C. Bøg-Hansen, and C.J.F. van Noorden. 1993. Biotin carboxylases in mitochondria
1135 and the cytosol from skeletal and cardiac muscle as detected by avidin binding. *Histochemistry*.
1136 100:415–421. doi:10.1007/BF00267821.

1137 Lavialle, M., G. Aumann, E. Anlauf, F. Pröls, M. Arpin, and A. Derouiche. 2011. Structural plasticity of
1138 perisynaptic astrocyte processes involves ezrin and metabotropic glutamate receptors. *Proc.*
1139 *Natl. Acad. Sci. U. S. A.* 108:12915–12919. doi:10.1073/pnas.1100957108.

1140 Lee, D.-E., J.E. Yoo, J. Kim, S. Kim, S. Kim, H. Lee, and H. Cheong. 2020. NEDD4L downregulates
1141 autophagy and cell growth by modulating ULK1 and a glutamine transporter. *Cell Death Dis.*
1142 11:1–17. doi:10.1038/s41419-020-2242-5.

1143 Lee, K.Y., K.A. Jewett, H.J. Chung, and N.-P. Tsai. 2018. Loss of fragile X protein FMRP impairs
1144 homeostatic synaptic downscaling through tumor suppressor p53 and ubiquitin E3 ligase Nedd4-
1145 2. *Hum. Mol. Genet.* 27:2805–2816. doi:10.1093/hmg/ddy189.

1146 Lee, Y., A. Messing, M. Su, and M. Brenner. 2008. GFAP promoter elements required for region-specific
1147 and astrocyte-specific expression. *Glia*. 56:481–493. doi:10.1002/glia.20622.

1148 Letellier, M., Z. Szíber, I. Chamma, C. Saphy, I. Papasideri, B. Tessier, M. Sainlos, K. Czöndör, and O.
1149 Thoumine. 2018. A unique intracellular tyrosine in neuroligin-1 regulates AMPA receptor
1150 recruitment during synapse differentiation and potentiation. *Nat. Commun.* 9:3979.
1151 doi:10.1038/s41467-018-06220-2.

1152 Li, J., T.G. Miramontes, T. Czopka, and K.R. Monk. 2024. Synaptic input and Ca2+ activity in zebrafish
1153 oligodendrocyte precursor cells contribute to myelin sheath formation. *Nat. Neurosci.*
1154 doi:10.1038/s41593-023-01553-8.

1155 Liu, X., H. Zhang, B. Zhang, J. Tu, X. Li, and Y. Zhao. 2021. Nedd4-2 haploinsufficiency in mice causes
1156 increased seizure susceptibility and impaired Kir4.1 ubiquitination. *Biochim. Biophys. Acta Mol.*
1157 *Basis Dis.* 1867:166128. doi:10.1016/j.bbadis.2021.166128.

1158 Loh, K.H., P.S. Stawski, A.S. Draycott, N.D. Udeshi, E.K. Lehrman, D.K. Wilton, T. Svinkina, T.J. Deerinck,
1159 M.H. Ellisman, B. Stevens, S.A. Carr, and A.Y. Ting. 2016. Proteomic Analysis of Unbounded
1160 Cellular Compartments: Synaptic Clefts. *Cell*. 166:1295-1307.e21.
1161 doi:10.1016/j.cell.2016.07.041.

1162 Minegishi, S., T. Ishigami, T. Kino, L. Chen, R. Nakashima-Sasaki, N. Araki, K. Yatsu, M. Fujita, and S.
1163 Umemura. 2016. An isoform of Nedd4-2 is critically involved in the renal adaptation to high salt
1164 intake in mice. *Sci. Rep.* 6:27137. doi:10.1038/srep27137.

1165 Molotkov, D., S. Zobova, J.M. Arcas, and L. Khiroug. 2013. Calcium-induced outgrowth of astrocytic
1166 peripheral processes requires actin binding by Profilin-1. *Cell Calcium*. 53:338–348.
1167 doi:10.1016/j.ceca.2013.03.001.

1168 Mukhopadhyay, D., and H. Riezman. 2007. Proteasome-independent functions of ubiquitin in
1169 endocytosis and signaling. *Science*. 315:201–205. doi:10.1126/science.1127085.

1170 Na, C.H., D.R. Jones, Y. Yang, X. Wang, Y. Xu, and J. Peng. 2012. Synaptic Protein Ubiquitination in Rat
1171 Brain Revealed by Antibody-based Ubiquitome Analysis. *J. Proteome Res.* 11:4722–4732.
1172 doi:10.1021/pr300536k.

1173 Nagaki, K., H. Yamamura, S. Shimada, T. Saito, S. Hisanaga, M. Taoka, T. Isobe, and T. Ichimura. 2006. 14-
1174 3-3 Mediates phosphorylation-dependent inhibition of the interaction between the ubiquitin E3
1175 ligase Nedd4-2 and epithelial Na+ channels. *Biochemistry*. 45:6733–6740.
1176 doi:10.1021/bi052640q.

1177 Nguyen, Q.-A., M.E. Horn, and R.A. Nicoll. 2016. Distinct roles for extracellular and intracellular domains
1178 in neuroligin function at inhibitory synapses. *eLife*. 5. doi:10.7554/eLife.19236.

1179 Oberheim, N.A., X. Wang, S. Goldman, and M. Nedergaard. 2006. Astrocytic complexity distinguishes the
1180 human brain. *Trends Neurosci.* 29:547–553. doi:10.1016/j.tins.2006.08.004.

1181 Parente, D.J., C. Garriga, B. Baskin, G. Douglas, M.T. Cho, G.C. Araujo, and M. Shinawi. 2017. Neuroligin 2
1182 nonsense variant associated with anxiety, autism, intellectual disability, hyperphagia, and
1183 obesity. *Am. J. Med. Genet. A.* 173:213–216. doi:10.1002/ajmg.a.37977.

1184 Perez-Riverol, Y., J. Bai, C. Bandla, D. García-Seisdedos, S. Hewapathirana, S. Kamatchinathan, D.J.
1185 Kundu, A. Prakash, A. Frericks-Zipper, M. Eisenacher, M. Walzer, S. Wang, A. Brazma, and J.A.
1186 Vizcaíno. 2022. The PRIDE database resources in 2022: a hub for mass spectrometry-based
1187 proteomics evidences. *Nucleic Acids Res.* 50:D543–D552. doi:10.1093/nar/gkab1038.

1188 Pirozzi, G., S.J. McConnell, A.J. Uveges, J.M. Carter, A.B. Sparks, B.K. Kay, and D.M. Fowlkes. 1997.
1189 Identification of novel human WW domain-containing proteins by cloning of ligand targets. *J.*
1190 *Biol. Chem.* 272:14611–14616. doi:10.1074/jbc.272.23.14611.

1191 Poulopoulos, A., G. Aramuni, G. Meyer, T. Soykan, M. Hoon, T. Papadopoulos, M. Zhang, I. Paarmann, C.
1192 Fuchs, K. Harvey, P. Jedlicka, S.W. Schwarzacher, H. Betz, R.J. Harvey, N. Brose, W. Zhang, and F.
1193 Varoqueaux. 2009. Neuroligin 2 Drives Postsynaptic Assembly at Perisomatic Inhibitory Synapses
1194 through Gephyrin and Collybistin. *Neuron*. 63:628–642. doi:10.1016/j.neuron.2009.08.023.

1195 Poulopoulos, A., T. Soykan, L.P. Tuffy, M. Hammer, F. Varoqueaux, and N. Brose. 2012.
1196 Homodimerization and isoform-specific heterodimerization of neuroligins. *Biochem. J.* 446:321–
1197 330. doi:10.1042/BJ20120808.

1198 Preman, P., M. Alfonso-Triguero, E. Alberdi, A. Verkhratsky, and A.M. Arranz. 2021. Astrocytes in
1199 Alzheimer's Disease: Pathological Significance and Molecular Pathways. *Cells*. 10:540.
1200 doi:10.3390/cells10030540.

1201 Rodrigues, D.C., M. Mufteev, R.J. Weatheritt, U. Djuric, K.C.H. Ha, P.J. Ross, W. Wei, A. Piekna, M.A.
1202 Sartori, L. Byres, R.S.F. Mok, K. Zaslavsky, P. Pasceri, P. Diamandis, Q. Morris, B.J. Blencowe, and
1203 J. Ellis. 2020. Shifts in Ribosome Engagement Impact Key Gene Sets in Neurodevelopment and
1204 Ubiquitination in Rett Syndrome. *Cell Rep.* 30:4179-4196.e11. doi:10.1016/j.celrep.2020.02.107.

1205 Rothstein, J.D., M. Van Kammen, A.I. Levey, L.J. Martin, and R.W. Kuncl. 1995. Selective loss of glial
1206 glutamate transporter GLT-1 in amyotrophic lateral sclerosis. *Ann. Neurol.* 38:73–84.
1207 doi:10.1002/ana.410380114.

1208 Roux, K.J., D.I. Kim, M. Raida, and B. Burke. 2012. A promiscuous biotin ligase fusion protein identifies
1209 proximal and interacting proteins in mammalian cells. *J. Cell Biol.* 196:801–810.
1210 doi:10.1083/jcb.201112098.

1211 Savage, J.T., J.J. Ramirez, W.C. Risher, Y. Wang, D. Irala, and C. Eroglu. 2024. SynBot is an open-source
1212 image analysis software for automated quantification of synapses. *Cell Rep. Methods*. 4:100861.
1213 doi:10.1016/j.crmeth.2024.100861.

1214 Scheiffele, P., J. Fan, J. Choih, R. Fetter, and T. Serafini. 2000. Neuroligin expressed in nonneuronal cells
1215 triggers presynaptic development in contacting axons. *Cell*. 101:657–669.

1216 Schnell, E., A.L. Bensen, E.K. Washburn, and G.L. Westbrook. 2012. Neuroligin-1 overexpression in
1217 newborn granule cells in vivo. *PloS One*. 7:e48045. doi:10.1371/journal.pone.0048045.

1218 Schnell, E., T.H. Long, A.L. Bensen, E.K. Washburn, and G.L. Westbrook. 2014. Neuroligin-1 knockdown
1219 reduces survival of adult-generated newborn hippocampal neurons. *Front. Neurosci.* 8.

1220 Shipman, S.L., and R.A. Nicoll. 2012. Dimerization of postsynaptic neuroligin drives synaptic assembly via
1221 transsynaptic clustering of neurexin. *Proc. Natl. Acad. Sci.* 109:19432–19437.
1222 doi:10.1073/pnas.1217633109.

1223 Shipman, S.L., E. Schnell, T. Hirai, B.-S. Chen, K.W. Roche, and R.A. Nicoll. 2011. Functional dependence
1224 of neuroligin on a new non-PDZ intracellular domain. *Nat. Neurosci.* 14:718–726.
1225 doi:10.1038/nn.2825.

1226 Singh, S.K., J.A. Stogsdill, N.S. Pulimood, H. Dingsdale, Y.H. Kim, L.-J. Pilaz, I.H. Kim, A.C. Manhaes, W.S.
1227 Rodrigues Jr., A. Pamukcu, E. Enustun, Z. Ertuz, P. Scheiffele, S.H. Soderling, D.L. Silver, R.-R. Ji,
1228 A.E. Medina, and C. Eroglu. 2016. Astrocytes Assemble Thalamocortical Synapses by Bridging
1229 NRX1α and NL1 via Hevin. *Cell*. 164:183–196. doi:10.1016/j.cell.2015.11.034.

1230 Soto, J.S., Y. Jami-Alahmadi, J. Chacon, S.L. Moye, B. Diaz-Castro, J.A. Wohlschlegel, and B.S. Khakh.
1231 2023. Astrocyte-neuron subproteomes and obsessive-compulsive disorder mechanisms. *Nature*.
1232 616:764–773. doi:10.1038/s41586-023-05927-7.

1233 Stogsdill, J.A., J. Ramirez, D. Liu, Y.H. Kim, K.T. Baldwin, E. Enustun, T. Ejikeme, R.-R. Ji, and C. Eroglu.
1234 2017. Astrocytic neuroligins control astrocyte morphogenesis and synaptogenesis. *Nature*.
1235 551:192–197. doi:10.1038/nature24638.

1236 Sudol, M., and T. Hunter. 2000. NeW Wrinkles for an Old Domain. *Cell*. 103:1001–1004.
1237 doi:10.1016/S0092-8674(00)00203-8.

1238 Sudol, M., K. Sliwa, and T. Russo. 2001. Functions of WW domains in the nucleus. *FEBS Lett.* 490:190–
1239 195.

1240 Sumita, K., Y. Sato, J. Iida, A. Kawata, M. Hamano, S. Hirabayashi, K. Ohno, E. Peles, and Y. Hata. 2007.
1241 Synaptic scaffolding molecule (S-SCAM) membrane-associated guanylate kinase with inverted
1242 organization (MAGI)-2 is associated with cell adhesion molecules at inhibitory synapses in rat
1243 hippocampal neurons. *J. Neurochem.* 100:154–166. doi:10.1111/j.1471-4159.2006.04170.x.

1244 Tan, C.X., D.S. Bindu, E.J. Hardin, K. Sakers, R. Baumert, J.J. Ramirez, J.T. Savage, and C. Eroglu. 2023. δ-
1245 Catenin controls astrocyte morphogenesis via layer-specific astrocyte-neuron cadherin
1246 interactions. *J. Cell Biol.* 222:e202303138. doi:10.1083/jcb.202303138.

1247 Tian, R., X. Wu, T.L. Hagemann, A.A. Sosunov, A. Messing, G.M. McKhann, and J.E. Goldman. 2010.
1248 Alexander Disease Mutant Glial Fibrillary Acidic Protein Compromises Glutamate Transport in
1249 Astrocytes. *J. Neuropathol. Exp. Neurol.* 69:335–345. doi:10.1097/NEN.0b013e3181d3cb52.

1250 Totland, M.Z., C.H. Bergsland, T.A. Fykerud, L.M. Knudsen, N.L. Rasmussen, P.W. Eide, Z. Yohannes, V.
1251 Sørensen, A. Brech, R.A. Lothe, and E. Leithe. 2017. E3 ubiquitin ligase NEDD4 induces
1252 endocytosis and lysosomal sorting of connexin43 to promote loss of gap junctions. *J. Cell Sci.*
1253 jcs.202408. doi:10.1242/jcs.202408.

1254 Varoqueaux, F., G. Aramuni, R.L. Rawson, R. Mohrmann, M. Missler, K. Gottmann, W. Zhang, T.C.
1255 Südhof, and N. Brose. 2006. Neuroligins determine synapse maturation and function. *Neuron*.
1256 51:741–754. doi:10.1016/j.neuron.2006.09.003.

1257 Venkatesh, H.S., T.B. Johung, V. Caretti, A. Noll, Y. Tang, S. Nagaraja, E.M. Gibson, C.W. Mount, J.
1258 Polepalli, S.S. Mitra, P.J. Woo, R.C. Malenka, H. Vogel, M. Bredel, P. Mallick, and M. Monje.
1259 2015. Neuronal Activity Promotes Glioma Growth through Neuroligin-3 Secretion. *Cell*. 161:803–
1260 816. doi:10.1016/j.cell.2015.04.012.

1261 Venkatesh, H.S., L.T. Tam, P.J. Woo, J. Lennon, S. Nagaraja, S.M. Gillespie, J. Ni, D.Y. Duveau, P.J. Morris,
1262 J.J. Zhao, C.J. Thomas, and M. Monje. 2017. Targeting neuronal activity-regulated neuroligin-3
1263 dependency in high-grade glioma. *Nature*. 549:533–537. doi:10.1038/nature24014.

1264 Verkhratsky, A., and M. Nedergaard. 2018. Physiology of Astroglia. *Physiol. Rev.* 98:239–389.
1265 doi:10.1152/physrev.00042.2016.

1266 Wagner, S.A., P. Beli, B.T. Weinert, C. Schölz, C.D. Kelstrup, C. Young, M.L. Nielsen, J.V. Olsen, C.
1267 Brakebusch, and C. Choudhary. 2012. Proteomic analyses reveal divergent ubiquitylation site
1268 patterns in murine tissues. *Mol. Cell. Proteomics MCP*. 11:1578–1585.
1269 doi:10.1074/mcp.M112.017905.

1270 Wu, T., E. Hu, S. Xu, M. Chen, P. Guo, Z. Dai, T. Feng, L. Zhou, W. Tang, L. Zhan, X. Fu, S. Liu, X. Bo, and G.
1271 Yu. 2021. clusterProfiler 4.0: A universal enrichment tool for interpreting omics data. *The*
1272 *Innovation*. 2:100141. doi:10.1016/j.xinn.2021.100141.

1273 Xie, H., S. Liu, Y. Fu, Q. Cheng, P. Wang, C.-L. Bi, R. Wang, M.-M. Chen, and M. Fang. 2023. Nuclear access
1274 of DNlg3 c-terminal fragment and its function in regulating innate immune response genes.
1275 *Biochem. Biophys. Res. Commun.* 641:93–101. doi:10.1016/j.bbrc.2022.12.030.

1276 Xie, Y., A.T. Kuan, W. Wang, Z.T. Herbert, O. Mosto, O. Olukoya, M. Adam, S. Vu, M. Kim, D. Tran, N.
1277 Gómez, C. Charpentier, I. Sorour, T.E. Lacey, M.Y. Tolstorukov, B.L. Sabatini, W.-C.A. Lee, and

1278 C.C. Harwell. 2022. Astrocyte-neuron crosstalk through Hedgehog signaling mediates cortical
1279 synapse development. *Cell Rep.* 38:110416. doi:10.1016/j.celrep.2022.110416.

1280 Xu, C., C.D. Fan, and X. Wang. 2015. Regulation of Mdm2 protein stability and the p53 response by
1281 NEDD4-1 E3 ligase. *Oncogene*. 34:281–289. doi:10.1038/onc.2013.557.

1282 Xu, J., Y. Du, J. Xu, X. Hu, L. Gu, X. Li, P. Hu, T. Liao, Q. Xia, Q. Sun, L. Shi, J. Luo, J. Xia, Z. Wang, and J. Xu.
1283 2019. Neuroligin 3 Regulates Dendritic Outgrowth by Modulating Akt/mTOR Signaling. *Front.*
1284 *Cell. Neurosci.* 13:518. doi:10.3389/fncel.2019.00518.

1285 Xu, N., R. Cao, S.-Y. Chen, X.-Z. Gou, B. Wang, H.-M. Luo, F. Gao, and A.-H. Tang. 2024. Structural and
1286 functional reorganization of inhibitory synapses by activity-dependent cleavage of neuroligin-2.
1287 *Proc. Natl. Acad. Sci.* 121:e2314541121. doi:10.1073/pnas.2314541121.

1288 Zhang, Y., K. Chen, S.A. Sloan, M.L. Bennett, A.R. Scholze, S. O'Keeffe, H.P. Phatnani, P. Guarnieri, C.
1289 Caneda, N. Ruderisch, S. Deng, S.A. Liddelow, C. Zhang, R. Daneman, T. Maniatis, B.A. Barres,
1290 and J.Q. Wu. 2014. An RNA-Sequencing Transcriptome and Splicing Database of Glia, Neurons,
1291 and Vascular Cells of the Cerebral Cortex. *J. Neurosci.* 34:11929–11947.
1292 doi:10.1523/JNEUROSCI.1860-14.2014.

1293 Zhang, Y., X. He, X. Meng, X. Wu, H. Tong, X. Zhang, and S. Qu. 2017. Regulation of glutamate
1294 transporter trafficking by Nedd4-2 in a Parkinson's disease model. *Cell Death Dis.* 8:e2574.
1295 doi:10.1038/cddis.2016.454.

1296 Zhou, R., S.V. Patel, and P.M. Snyder. 2007. Nedd4-2 catalyzes ubiquitination and degradation of cell
1297 surface ENaC. *J. Biol. Chem.* 282:20207–20212. doi:10.1074/jbc.M611329200.

1298

1299

1300 **FIGURE LEGENDS**

1301 **Figure 1: Astrocytic Neuroligins 1, 2, and 3 have non-redundant roles in**

1302 **morphogenesis.**

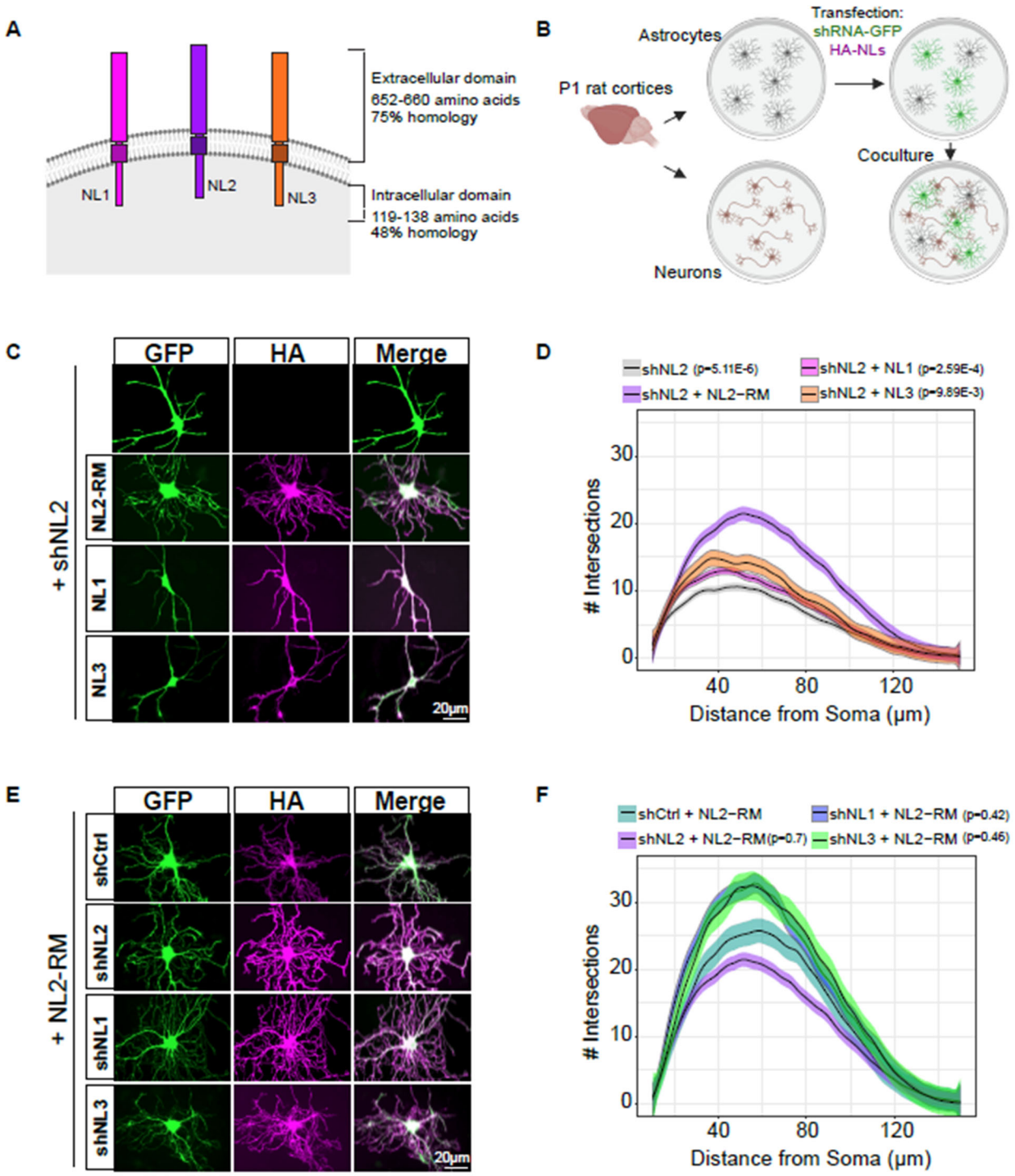

1303

1304 A) Cartoon depiction of NLs 1-3. Length and homology refer to mouse sequences.

1305 B) Neuron-astrocyte co-culture method to study astrocyte morphogenesis in vitro. P1 rat
1306 cortices are used to isolate astrocytes and neurons separately to allow for astrocyte-
1307 specific gene manipulation. Astrocytes post-transfection are plated onto neurons for 48h
1308 to allow arborization.

1309 C) Representative images of astrocytes transfected with shNL2 and either: HA-NL2-RM
1310 (Rescue mutant, resistant to shRNA), HA-NL1, or HA-NL3. Scale bars are 20μm.

1311 D) Sholl analysis quantification of conditions shown in C. Linear-mixed model followed
1312 by ANOVA reveals main effect of condition $F(3, 12) = 9.074$, $p = 0.0021$. P-values
1313 represent Dunnett's post-hoc with respect to the shNL2+HA-NL2-RM condition. N = 48-
1314 96 cells per condition, across >3 independent culture experiments. Statistical analysis
1315 was performed using the biological replicate (independent cultures) N to avoid
1316 pseudoreplication artifacts.

1317 E) Representative images of astrocytes co-transfected with shRNA against either NL1,
1318 NL2, or NL3, and HA-NL2-RM. Scale bars are 20μm.

1319 F) Sholl analysis quantification of conditions in E. Linear-mixed model followed by
1320 ANOVA reveals trending effect of condition $F(3, 11)=3.15$, $p=0.0686$. P-values
1321 represent Dunnett's post-hoc with respect to shCtrl+NL2-RM. N = 53-97 cells per
1322 condition, across 3 independent culture experiments. Statistical analysis was performed
1323 using the biological replicate (independent cultures) N to avoid pseudoreplication
1324 artifacts. Note that the shNL2 + HA-NL2 data is the same across D and F.

1325 **Figure 2: The intracellular WW-binding motifs of Neuroligins uniquely regulate**

1326 **astrocyte morphology.**

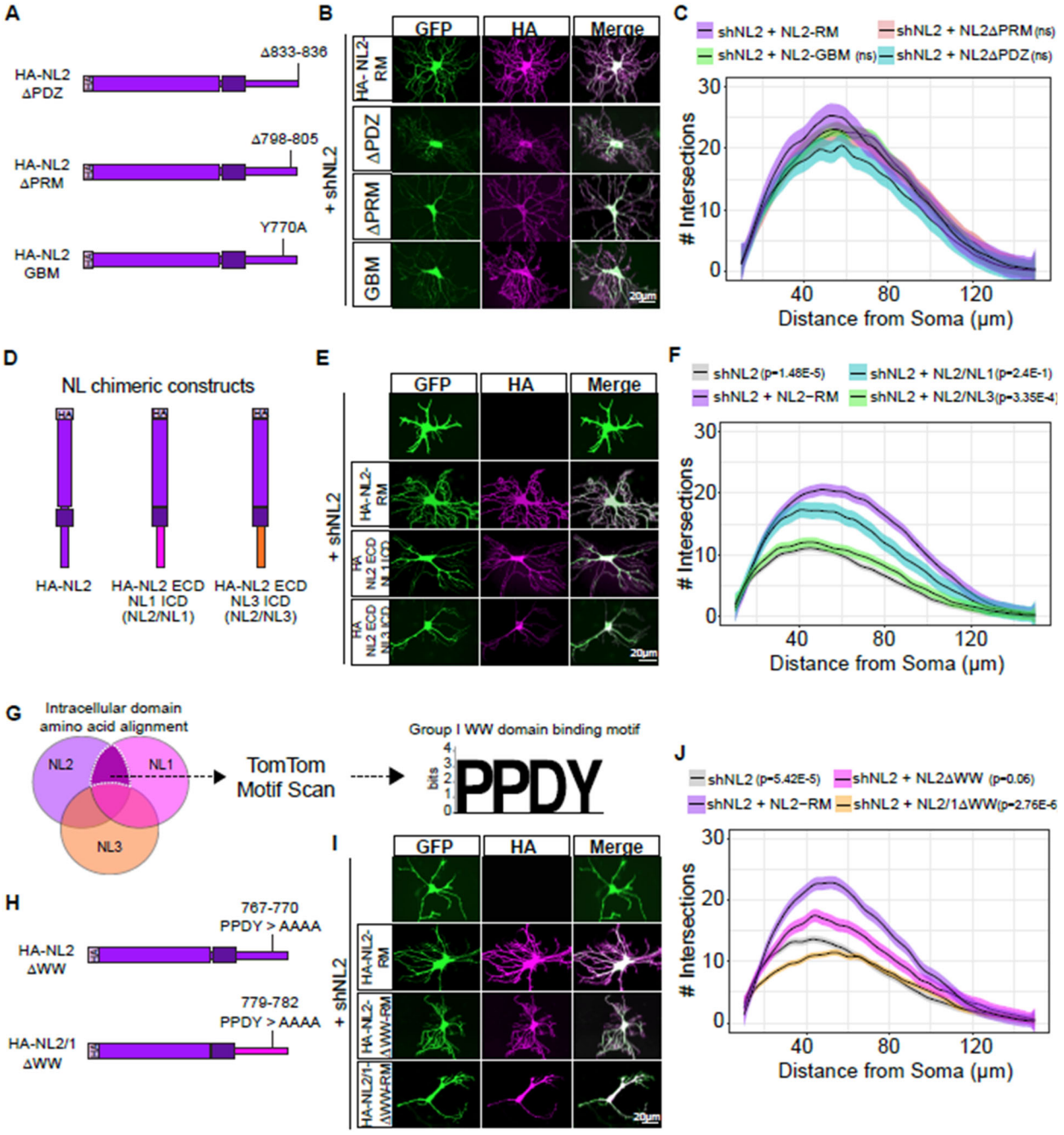

1327

1328 A) Cartoon of NL2 intracellular domain mutants.

1329 B) Representative images of astrocytes co-transfected with shNL2 and either HA-NL2-
1330 RM (Rescue Mutant, resistant to shRNA) or mutants lacking known motifs. Scale bars
1331 are 20μm.

1332 C) Sholl analysis quantification of the conditions in D. Linear-mixed model followed by
1333 ANOVA reveals no effect of condition $F(3, 8)=0.32$, $p=0.81$. NS = not significant in
1334 Dunnett's post-hoc. N=36-46 cells per condition, across 3 independent culture
1335 experiments. Statistical analysis was performed using the biological replicate
1336 (independent cultures) N to avoid pseudoreplication artifacts.

1337 D) Cartoon of NL2-ECD and NL1 or 3 ICD chimeric constructs.

1338 E) Representative images of astrocytes transfected with shNL2 and either HA-NL2-RM
1339 (Rescue mutant, resistant to shRNA), or chimeric proteins: HA-NL2(ECD)-NL1(ICD),
1340 HA-NL2(ECD)-NL3(ICD). Scale bars are 20μm.

1341 F) Sholl analysis quantification of conditions in B. Linear-mixed model followed by
1342 ANOVA reveals the main effect of condition $F(3,12)=8.8$, $p=0.0023$. P-values represent
1343 Dunnett's post-hoc with respect to shNL2+NL2-RM. N=57-97 cells per condition, across
1344 4 independent culture experiments. Statistical analysis was performed using the
1345 biological replicate (independent cultures) N to avoid pseudoreplication artifacts.

1346 G) Venn diagram depicting the overlap of sequences in NL1, NL2, and NL3 ICDs used
1347 for motif scanning by TomTom. We identified the motif PPDY which is common between
1348 NL1 and NL2 but absent in NL3.

1349 H) Cartoon of NL2ΔWW and NL2/1ΔWW mutant constructs.

1350 I) Representative images of astrocytes transfected with shNL2 and HA-NL2-RM-ΔWW
1351 or shNL2 and HA-NL2/1-ΔWW. Scale bars are 20μm.

1352 J) Sholl analysis quantification of conditions in F. Linear-mixed model ANOVA reveals
1353 the main effect of condition $F(3, 13)=9.9$, $p=0.0011$. P-values represent Dunnett's
1354 posthoc with respect to shNL2+NL2-RM. N = 71-84 cells per condition, across 4
1355 independent culture experiments. Statistical analysis was performed using the biological
1356 replicate (independent cultures) N to avoid pseudoreplication artifacts.

1357

1358 **Figure 3: *In vivo* Neuroligin BioID.**

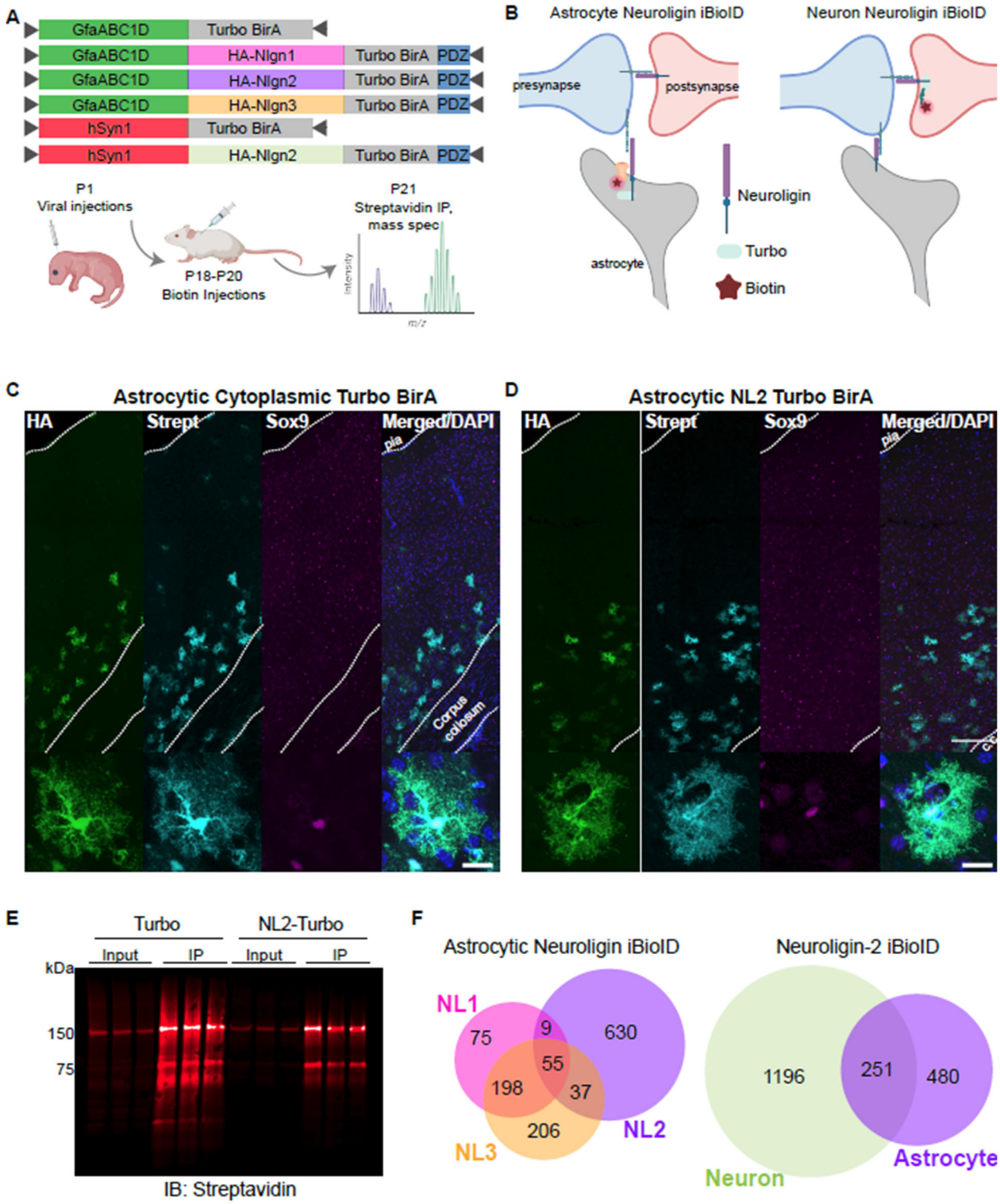

1359

1360 A) Schematic of AAV constructs and the experimental strategy of in vivo BioID to
1361 identify NL interactome *in vivo*. Each biological replicate contained two pooled cortices,
1362 3 biological replicates per condition.

1363 B) Cartoon depiction of Neuroligin iBioID constructs in astrocytes or neurons.

1364 C-D). Representative cortical images of Astrocytic Turbo BirA (C) or Astrocytic NL2
1365 Turbo BirA (D) injected animals. Stained with Streptavidin-594 (Strept), HA and Sox9 to
1366 determine astrocyte specificity. Scale bars: column image = 100μm; inset = 20μm.

1367 E) Representative western blot of iBioID immunoprecipitation from astrocytic Turbo vs
1368 NL2-Turbo animals demonstrates successful enrichment of biotinylated proteins in
1369 immunoprecipitation. Input is 2% of total cortex homogenate. IP is 15% of the eluate
1370 sample. Prominent bands are expected at approximately 150 and 75kDa which
1371 represent mitochondrial carboxylases(Kirkeby et al., 1993) [blot is overexposed to show
1372 this in the input lanes]. Resulting 'smear' in IP lanes indicated various-sized proteins
1373 that have been biotinylated near the bait protein.

1374 F) Venn diagram of protein interactors across astrocytic NL1, NL2, and NL3 and
1375 astrocytic versus neuronal NL2.

1376 **Figure 4: Neuroligin iBioID reveals novel intracellular domain interacting proteins.**

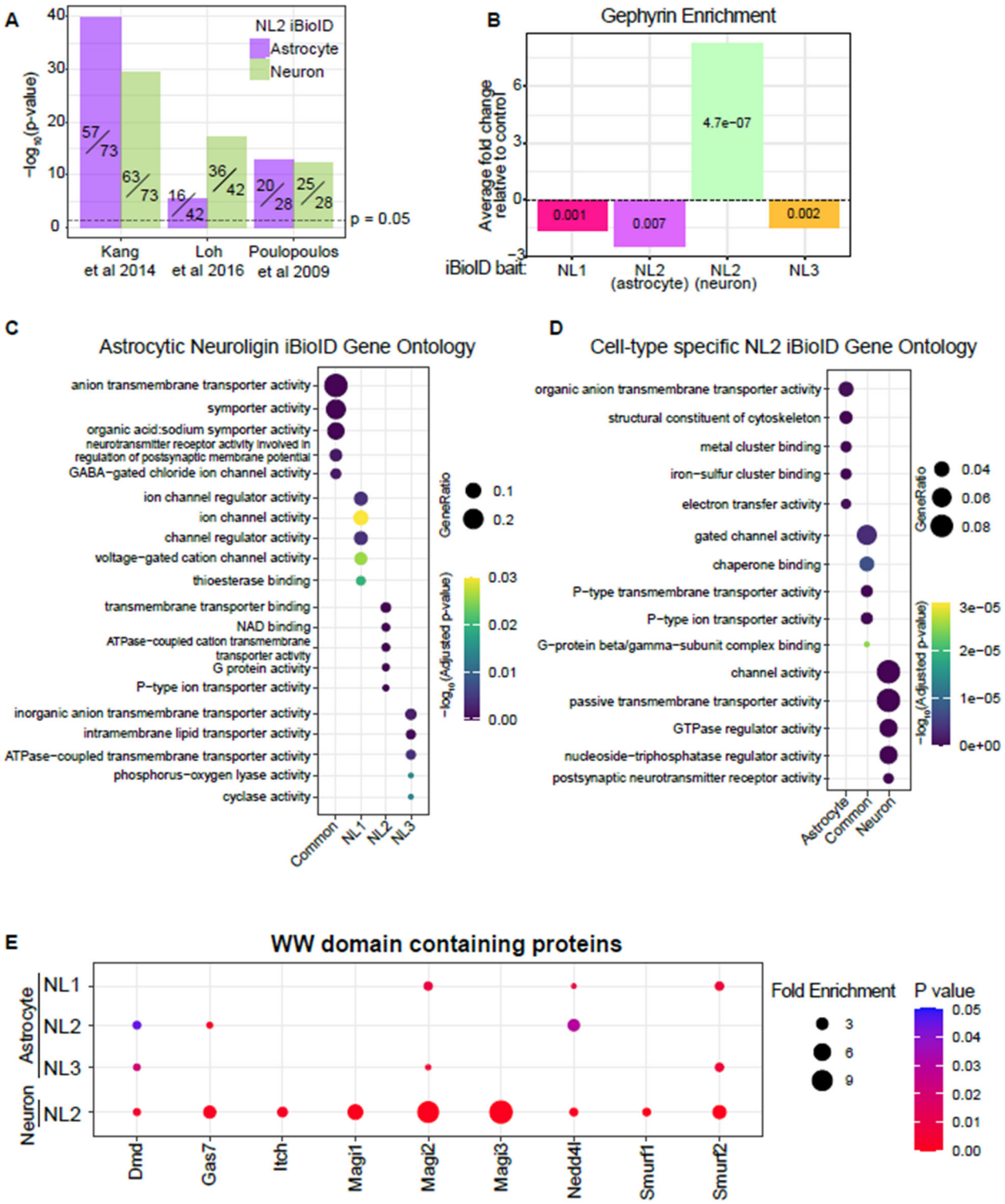

1377

1378 A) Enrichment of NL2 iBioID datasets with previously published datasets of NL2-
1379 interacting proteins. P-values are the result of Fisher's exact test. The number on the
1380 bars indicates the number of proteins from appropriate NL2 iBioID that are found in the
1381 published dataset.

1382 B) Gephyrin enrichment with each NL iBioID. Enrichment is defined as fold change bait /
1383 cytosolic control (Turbo BirA). P values are the results of t-tests within each experiment.

1384 C) Top 5 Gene Ontology Biological Processes categories for each NL BioID. Common
1385 indicates proteins found in astrocytic NL1, NL2, and NL3 iBioID. The complete gene
1386 ontology list can be found in Datset S2. GeneRatio indicates number of gene names
1387 (from the input iBioID protein list) in the GO category, out of all gene names in that
1388 category. Input for the analysis was proteins from iBioID lists that were at least 1.5 fold
1389 enriched at a p-value of <0.05, compared to respective controls.

1390 D) Top 5 Gene Ontology Biological Processes categories for each Neuronal or
1391 Astrocytic NL2 BioID. Common indicates proteins found in both astrocytic NL2 and
1392 neuronal NL2 iBioID. The complete gene ontology list can be found in Dataset S2.
1393 GeneRatio indicates number of gene names (from the input iBioID protein list) in the GO
1394 category, out of all gene names in that category. Input for the analysis was proteins
1395 from iBioID lists that were at least 1.5 fold enriched at a p-value of <0.05, compared to
1396 respective controls.

1397 E) All identified WW-binding protein interactors in iBioID experiments. Fold change is
1398 the enrichment of the interaction with the bait compared to cytosolic Turbo BirA alone,
1399 per cell type. P-value represents a two-tailed T-test compared to soluble Turbo BirA, per

1400 cell type. Input for the analysis was proteins from iBioID lists that were at least 1.5 fold

1401 enriched at a p-value of <0.05, compared to respective controls.

1402 **Figure 5: WW domain-containing proteins are necessary for astrocyte**

1403 **morphogenesis in vitro.**

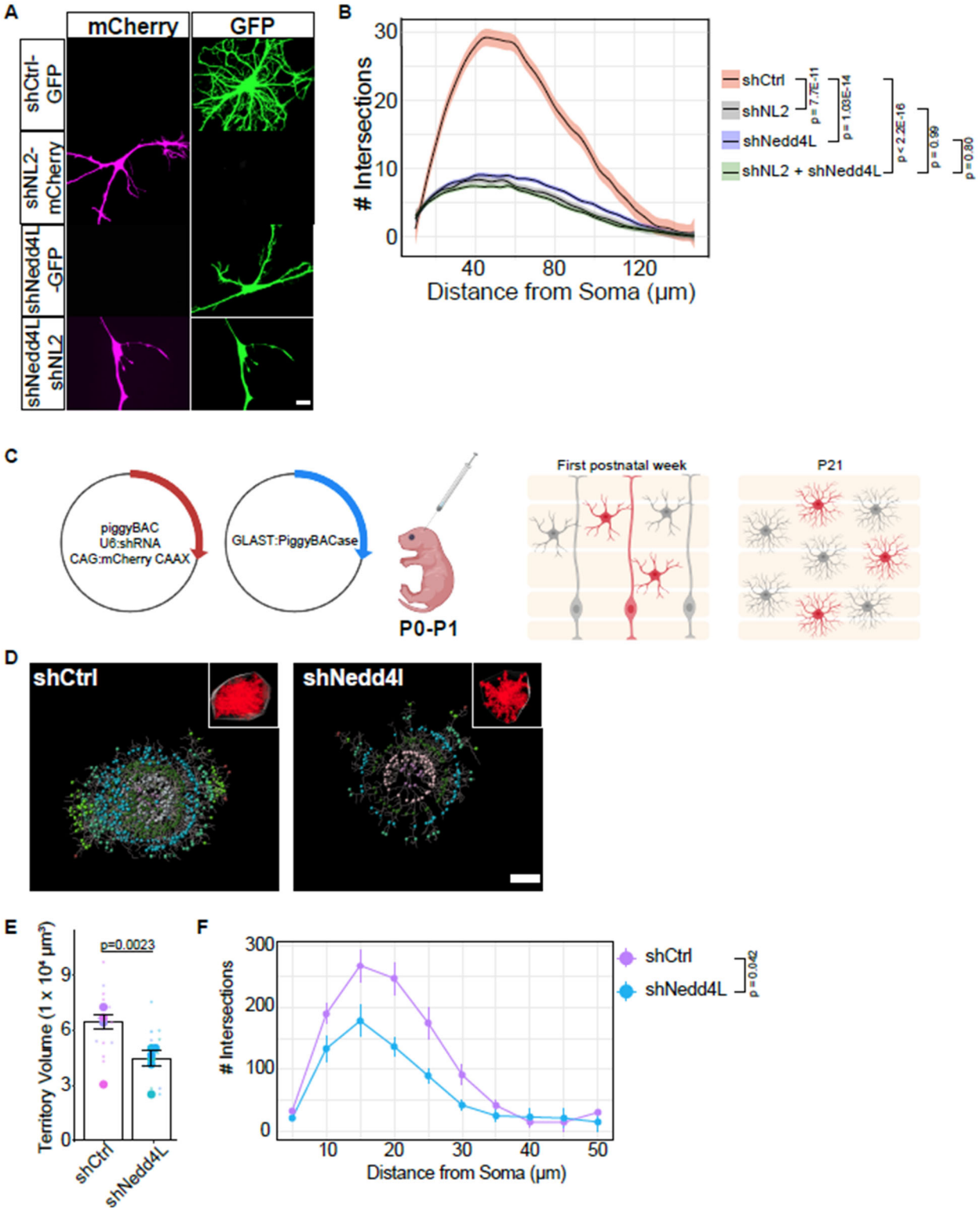

1404

1405 A) Representative images of astrocytes transfected with either a control shRNA
1406 (scrambled NL2 shRNA), an shRNA targeting Nedd4l (also expressing GFP) or shNL2
1407 (also expressing mCherry), or in combination. Astrocytes are cultured on top of neurons
1408 (not labeled). Scale bar is 20μm.

1409 B) Sholl analysis of the conditions in A. Linear-mixed model ANOVA reveals the main
1410 effect of condition F(3, 13)=38.104, p=1.05E-6. P-values on the graph represent
1411 Tukey's posthoc comparison to shCtrl. N = 60-100 cells per condition, across 4
1412 independent culture experiments. Statistical analysis was performed using the biological
1413 replicate (independent cultures) N to avoid pseudoreplication artifacts.

1414 C) Cartoon of postnatal astrocyte labeling by electroporation (PALE). Two plasmids
1415 (U6:shRNA and CAG:mCherry CAAX flanked by piggyBAC transposons, and GLAST:
1416 piggyBACase transposase) are electroporated into late P0 or early P1 mouse lateral
1417 ventricles. Brains are collected at P21 and stained for mCherry to visualize astrocyte
1418 territories.

1419 D) Imaris reconstructions of *in vivo* astrocyte territory volumes (inset) and 3D Sholl
1420 analysis of mouse cortical astrocytes. 'Filament' cytoskeletal structure is shown with
1421 grey lines, while spheres indicate 3D Sholl concentric circles [different colors indicate
1422 different distances from the nucleus]. Scale bars = 10μm.

1423 E) Territory volume super plot quantification of the conditions in C. Large dots on graph
1424 = average per animal. Smaller dots = individual cells. Data were analyzed using a
1425 nested ANOVA; main effect of condition, F(1, 8) = 11.95, p=0.0023. The same cells
1426 were measured for territory volume and Sholl analysis. N=14-18 cells across 4-7

1427 animals (biological replicates) per condition. Statistical analysis was performed on the
1428 biological replicate number and not the number of cells to avoid pseudoreplication
1429 artifacts.

1430 F) 3D Sholl analysis. Linear mixed model ANOVA $F(1,9)=5.59$, $p=0.0424$. The same
1431 cells were measured for territory volume and Sholl analysis. N=14-18 cells across 4-7
1432 animals (biological replicates) per condition. Statistical analysis was performed on the
1433 biological replicate number and not the number of cells to avoid pseudoreplication
1434 artifacts.

1435 **Figure 6: Nedd4l binding to Neuroligins is modulated by intracellular PPxY motifs.**

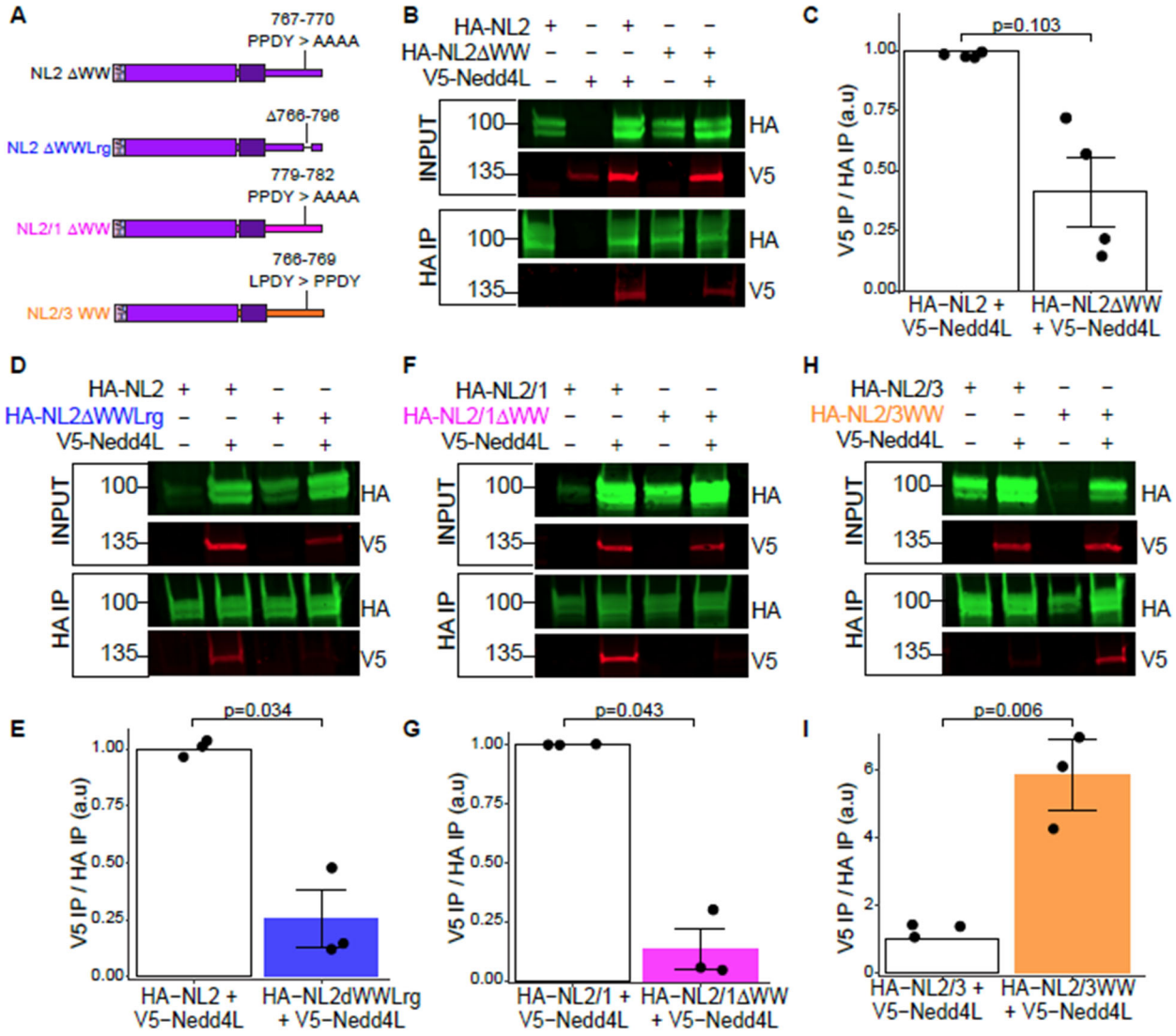

1436

1437 A) Cartoon of NL2 and NL2-ICD chimeric constructs. Numbers indicate amino acid

1438 positions in mouse sequence.

1439 B) Western blots from HEK cell lysates transfected with HA-NL2 or HA-NL2ΔWW with

1440 or without V5-Nedd4l constructs. Co-immunoprecipitation (IP) of V5-Nedd4l was

1441 detected with NL2-HA constructs using Li-Cor fluorescent imaging.

1442 C) Densitometry quantification of IP signal from conditions in B. N=4 biological
1443 replicates. P-values represent results of paired, Student's t-test.

1444 D) Western blots from HEK cell lysates transfected with HA-NL2 or HA-NL2ΔWWLrg
1445 (Deletion of amino acids 766-796) with or without V5-Nedd4l constructs. Co-
1446 immunoprecipitation (IP) of V5-Nedd4l was detected with NL2-HA constructs using Li-
1447 Cor fluorescent imaging.

1448 E) Densitometry quantification of IP signal from conditions in D. N=3 biological
1449 replicates (independent culture experiments). P-values represent results of paired,
1450 Student's t-test.

1451 F) Western blots from HEK cell lysates transfected with HA-NL2/1 or HA-NL2/1ΔWW
1452 with or without V5-Nedd4l constructs.

1453 G) Densitometry quantification of IP signal from conditions in F. N=3 biological
1454 replicates. P-values represent results of paired, Student's t-test.

1455 H) Western blots from HEK cell lysates transfected with HA-NL2/3 or HA-NL2/3-WW
1456 with or without V5-Nedd4l constructs.

1457 I) Densitometry quantification of IP signal from conditions in H. N=3 biological replicates.
1458 P-values represent results of paired, Student's t-test.

1459 (B, D, F, H) All western blots were run at least 3 times with independent samples. Note
1460 that Nedd4l (V5) blots were run separately (eluate divided evenly) to avoid bleed-
1461 through from the strong HA signal.

1462

1463 **Figure 7: Nedd4l stabilizes Neuroligin-2 via ubiquitination at K749R.**

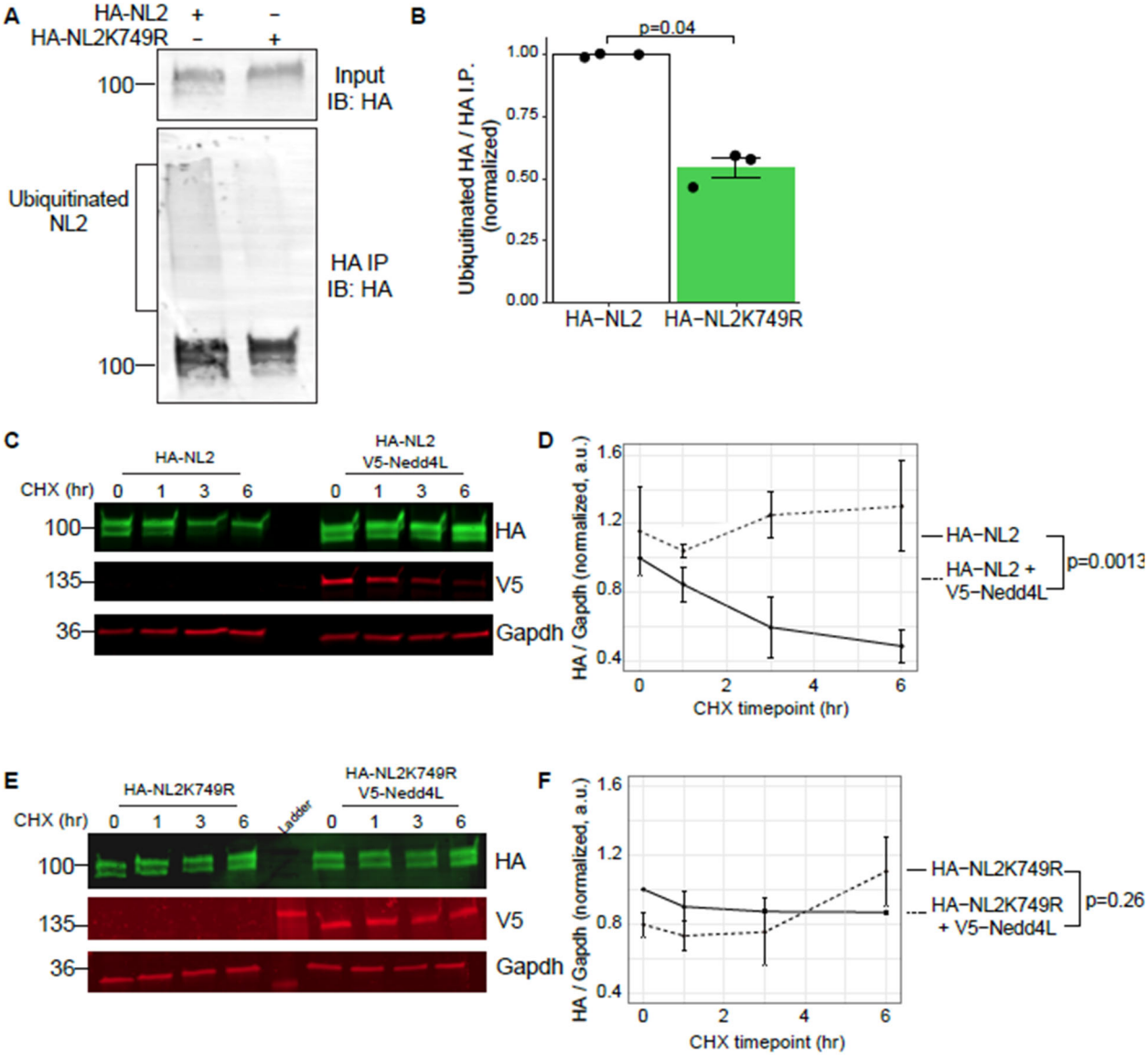

1464

1465 A) Western blot from rat primary astrocyte cell lysates and HA-NL2 IPs shows NL2 is

1466 ubiquitinated in astrocytes, which is lost when NL2 K749 is mutated to arginine

1467 (K749R). Input is 2% of total lysate.

1468 B) Quantification of HA ubiquitination signal from conditions in A. The ubiquitinated HA

1469 bands >100kDa were quantified via densitometry and normalized to the HA IP band

1470 (~100kDa) per biological replicate. N=3 biological replicates (independent culture
1471 experiments). P-values represent results of paired, Student's t-test.

1472 C) Western blots from HEK cell lysates transfected with HA-NL2 or HA-NL2 + V5-
1473 Nedd4l and treated with CHX. Numbers above the blot indicate hours after CHX
1474 treatment.

1475 D) Quantification of the conditions in B. Samples were collected on N=3 independent
1476 samples. Two-way ANOVA reveals main effect of condition $F(1, 16)=15.018$,
1477 $p=0.00134$, with no significant effect of time-point $F(3, 16)=0.41$, $p=0.74827$ or
1478 interaction $F(3, 16)=2.242$, $p=0.123$.

1479 E) Western blots from HEK cell lysates transfected with HA-NL2K749R or HA-
1480 NL2K749R + V5-Nedd4l and treated with CHX. Numbers above the blot indicate hours
1481 after CHX treatment.

1482 F) Quantification of the conditions in D. Samples were collected on N=3 independent
1483 samples. Two-way ANOVA reveals no significant effect of condition $F(1, 16)=1.392$,
1484 $p=0.255$, time-point $F(3, 16)=1.681$, $p=0.211$ or interaction $F(3, 16)=2.328$, $p=0.113$.

1485

1486 **Figure 8: Neuroligin-2 ubiquitination at K749 is critical for astrocyte**

1487 **morphogenesis.**

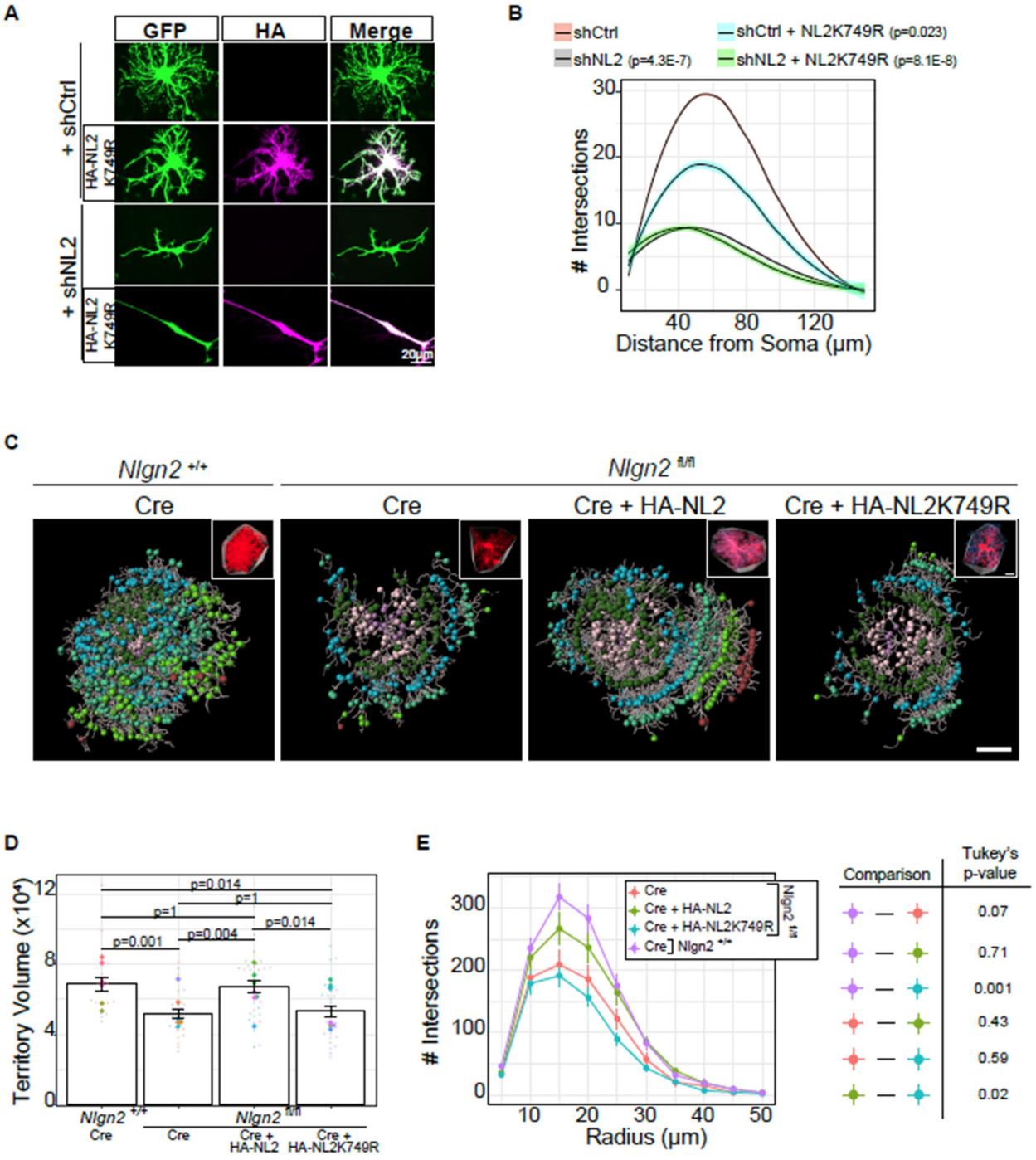

1488

1489 A) Representative images of astrocytes transfected with either shCtrl or shNL2 with or
1490 without HA-NL2K749R expression. Scale bars are 20μm.

1491 B) Sholl analysis quantification of images in J. Linear-mixed model ANOVA reveals the
1492 main effect of condition $F(3, 8)=13.49$, $p=0.0017$. P-values represent Dunnett's posthoc
1493 with respect to shCtrl. N = 62-80 cells per condition, across 3 independent culture
1494 experiments.

1495 C) Representative images of reconstructed astrocytes. 'Filament' cytoskeletal structure
1496 is shown with grey lines, while spheres indicate 3D Sholl concentric circles [different
1497 colors indicate different distances from the nucleus]. Insets show the astrocyte signal
1498 [tdTomato signal in red; HA signal in cyan] with the convex hull [grey surface lines].
1499 Scale bar = 10μm.

1500 D) Territory volume super plot quantification of the conditions in C. Large dots on graph
1501 = average per animal. Smaller dots = individual cells. Data were analyzed using
1502 Kruskal-Wallis rank sum test: $\chi^2 = 19.5$, $df=3$, $p=0.00013$. P-values on the graph are
1503 results of the Wilcoxon rank sum post hoc tests with Holm-Šídák multiple comparison
1504 correction. The same cells were measured for territory volume and Sholl analysis.
1505 N=21-33 cells across 6-7 animals (biological replicates) per condition.

1506 E) 3D Sholl analysis. Linear mixed model ANOVA $F(3, 105)=5.46$, $p=0.0016$. P-values
1507 in the table represent Tukey's post hoc tests. The same cells were measured for
1508 territory volume and Sholl analysis. N=21-33 cells across 6-7 animals (biological
1509 replicates) per condition.

1510

1511 **Supplemental Figure 1:**

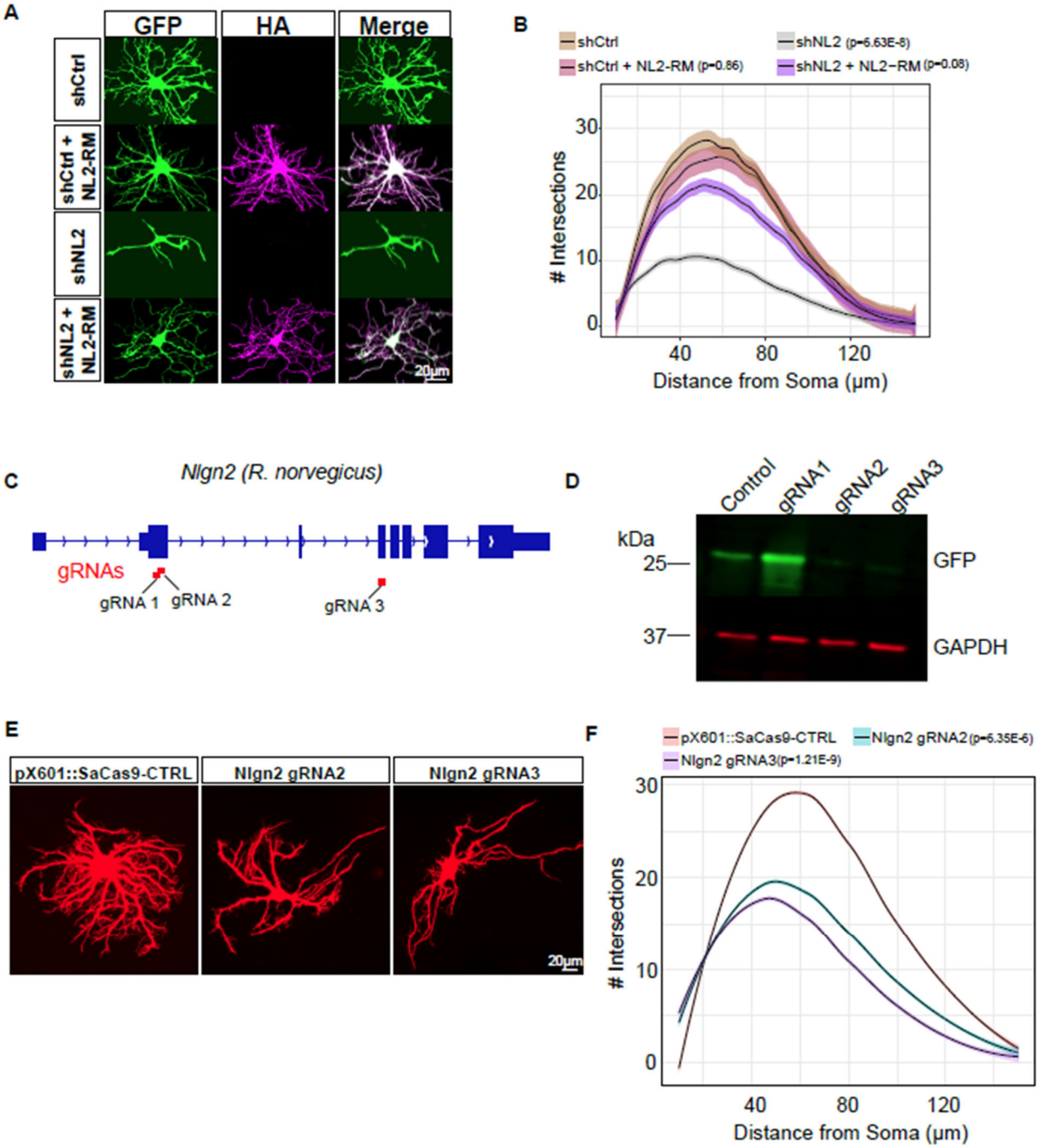

1512

1513 A) Representative images of astrocytes cultured on neurons. Astrocytes were

1514 transfected with either shCtrl or shNL2, alone or with HA-NL2-RM (Rescue mutant).

1515 B) Sholl analysis of images represented in A. Linear-mixed model followed by ANOVA
1516 reveals the main effect of condition $F(3, 10)=12.145$, $p=0.0011$. P-values represent post
1517 hoc Dunnett's comparison to shCtrl. N = 53-96 cells per condition, across 3 biological
1518 replicates (independent culture experiments).

1519 C) *Nlgn2* sequence illustrating location of the gRNAs using in D and E.

1520 D) Western blot of GFP translation assay. The target sequence of the gRNAs is cloned
1521 upstream and in-frame with GFP. gRNAs are co-expressed and then lysates are
1522 collected and run in equal protein load on an SDS-PAGE. The western blot was probed
1523 for GFP and GAPDH, for normalization.

1524 E) Representative images of astrocytes cultured on neurons. Astrocytes were
1525 transfected with pX601 (U6 gRNA GfaABC1D Cas9 T2A mCherry) prior to culturing on
1526 neurons.

1527 F) Sholl analysis of images represented in C. Linear-mixed model followed by ANOVA
1528 reveals the main effect of condition $F(2, 6) = 21.12$, $p=0.0019$. P-values represent post
1529 hoc Tukey's comparison to shCtrl. N = 40 cells per condition, across 3 biological
1530 replicates (independent culture experiments).

1531 **Supplemental Figure 2:**

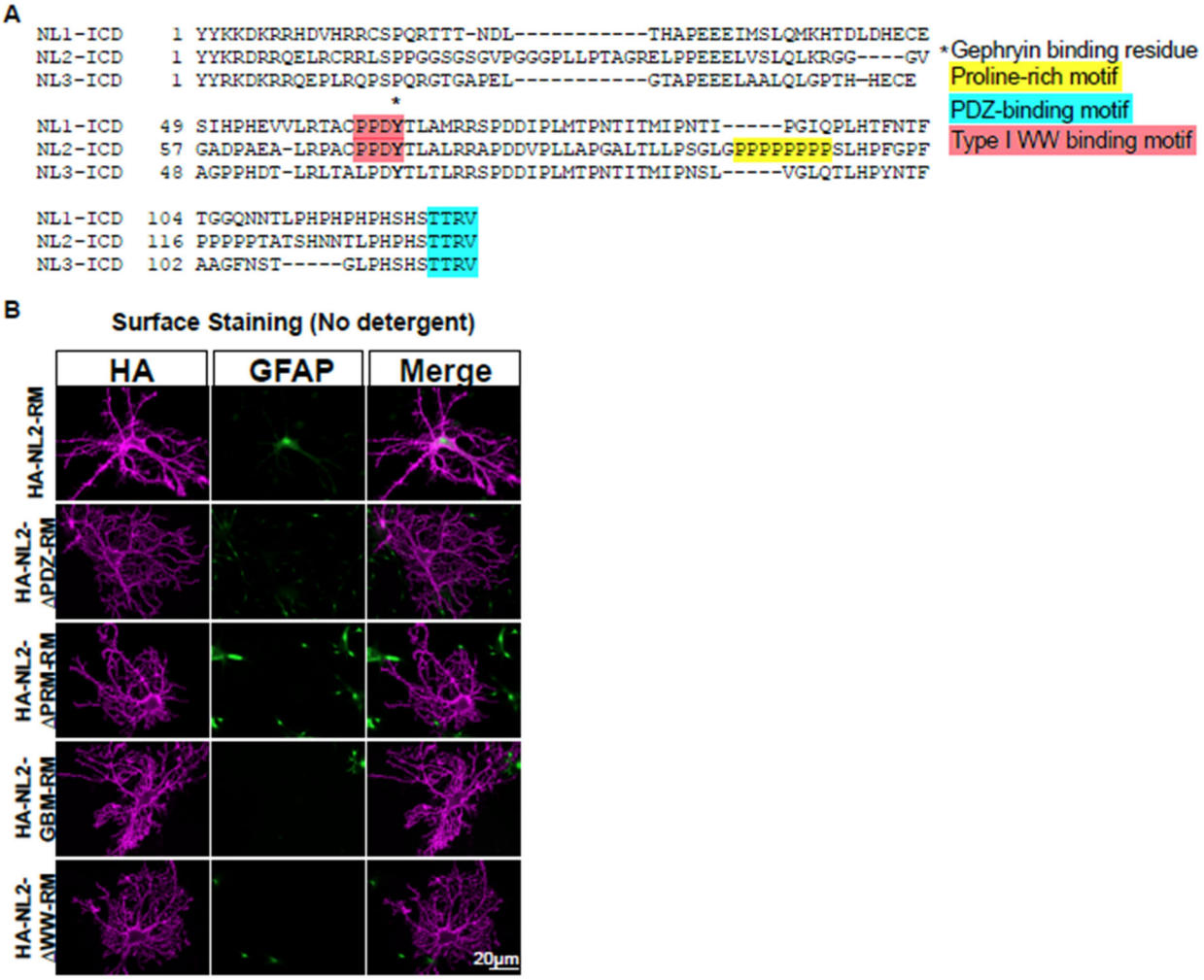

1532

1533 A) Mouse Neuroligin intracellular domain alignment, highlighting relevant protein

1534 sequence motifs.

1535 B) Representative images of surface-stained astrocyte/neuron co-cultures. Cells were

1536 fixed with cold 4% PFA for 5 minutes, and triton was omitted from blocking steps to

1537 avoid intracellular staining. GFAP was used as a negative control. HA (magenta) signal

1538 shows membrane localization as expected. GFAP signal is largely absent in the

1539 absence of detergent.

1540 **Supplemental Figure 3:**

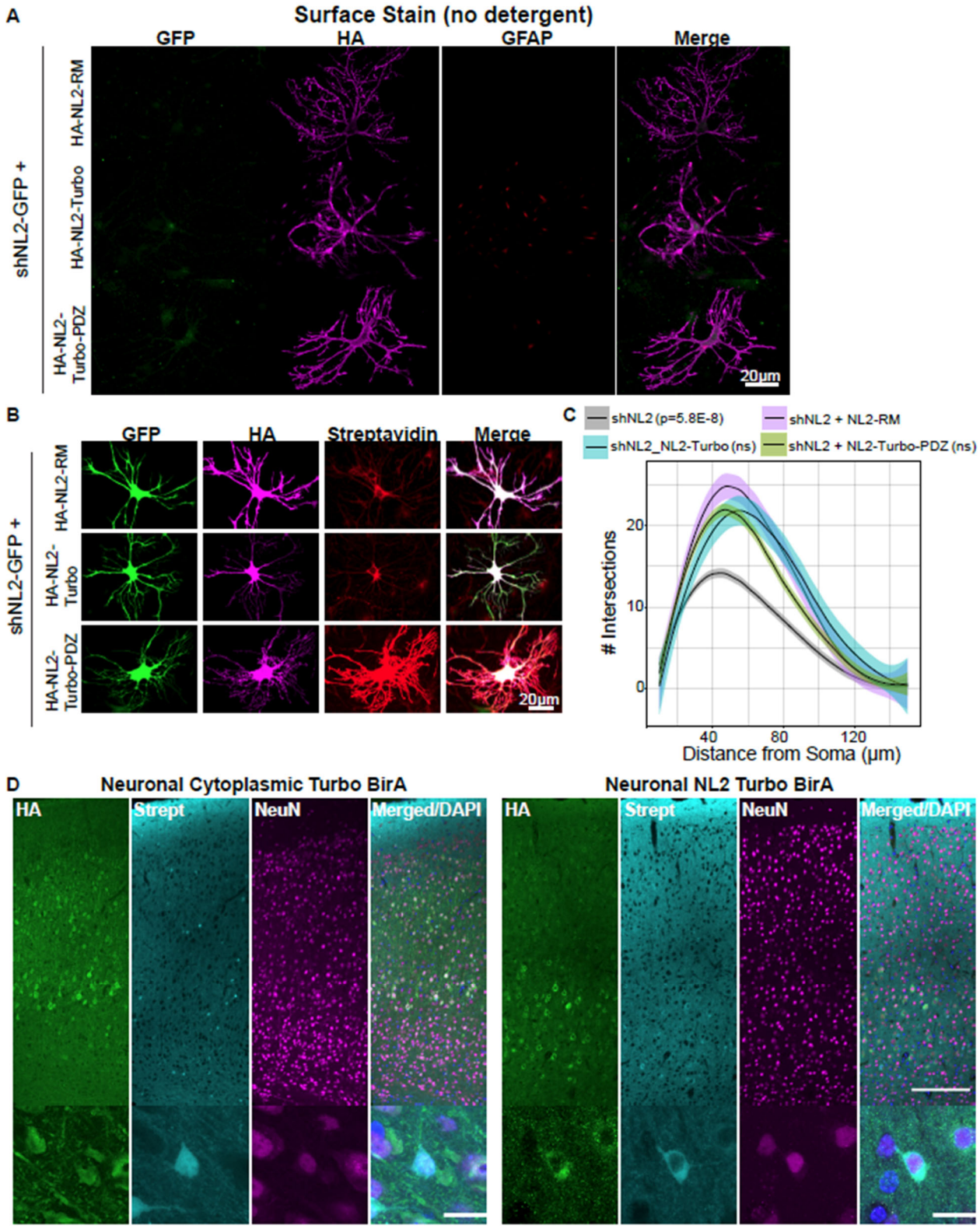

1541

1542 A) Representative images of surface-stained astrocyte/neuron co-cultures. Cells were
1543 fixed with cold 4% PFA for 5 minutes, and triton was omitted from blocking steps to
1544 avoid intracellular staining. GFP and GFAP were used as negative controls. HA
1545 (magenta) signal shows membrane localization as expected.

1546 B) Representative images demonstrating effective biotinylation (Streptavidin Alexa 594,
1547 red) in HA-NL2-Turbo-PDZ but not in HA-NL2 (negative control) or HA-NL2-Turbo.
1548 Experiments were performed at least twice with at least 20 cells per condition.

1549 C) Sholl analysis quantification of images in B. Linear-mixed model reveals the main
1550 effect of condition, $F(1,3)=11.01$, $p=1.4E-6$. P-values represent Dunnett's post-hoc with
1551 respect to shNL2 + NL2-RM. NS = not significant in Dunnett's. N = 14-56 cells across 3
1552 biological replicates (independent culture experiments).

1553 D). Representative cortical images of Neuronal Turbo BirA injected animals. Stained
1554 with Streptavidin-594 (Strept), HA and NeuN to determine neuronal specificity. Scale
1555 bars: column image = 100μm; inset = 20μm.

Supplemental Figure 4:

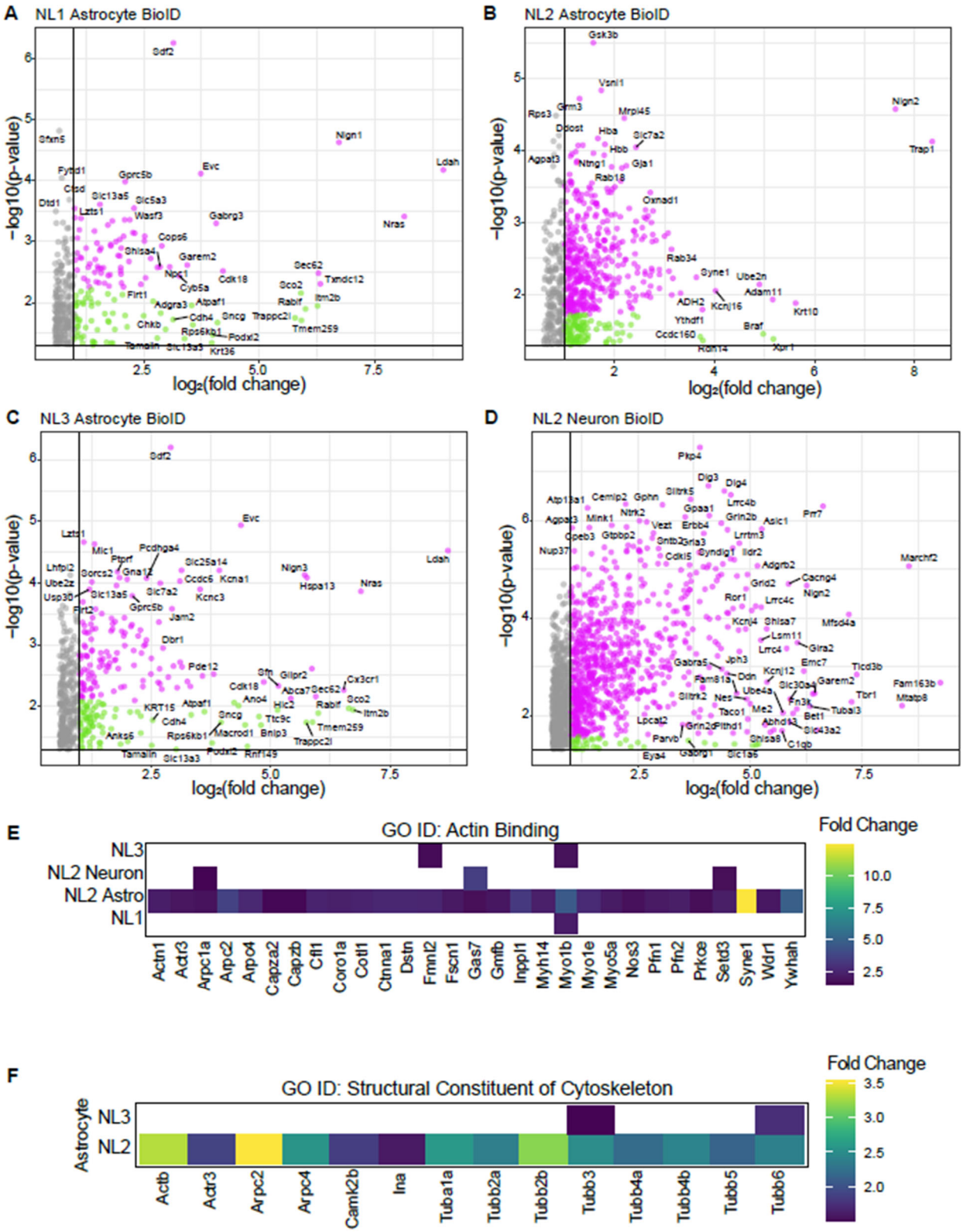

1558 A-D) Volcano plots of all proteins identified in the iBioID experiments. Pink dots indicate
1559 proteins enriched over cytoplasmic control with a fold change > 1.5 and an FDR-
1560 corrected p-value < 0.05. Green dots indicate proteins enriched over cytoplasmic control
1561 with a fold change > 1.5 and a p-value < 0.05.

1562 E-F) Expression of genes related to Actin Binding (E) or Structural Constituent of
1563 Cytoskeleton (F) from Gene Ontology analysis of iBioID shows that astrocytic NL2
1564 significantly interacts with cytoskeletal genes, compared to astrocyte NL1/NL3 or
1565 neuronal NL2.

1566 **Supplemental Figure 5:**

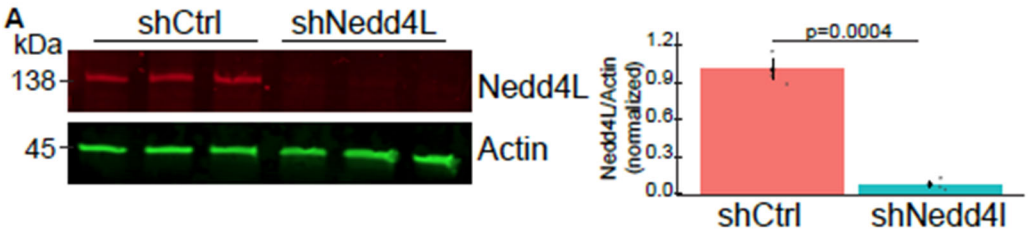

1567

1568 A) *left:* Western blots of astrocytes treated with lentivirus expressing shCtrl (scrambled

1569 shRNA) or shNedd4l. *Right:* Densitometry quantification [ImageJ]. The p value

1570 represents the results of the Student's t-test.

1571

1572 **Supplemental Figure 6:**

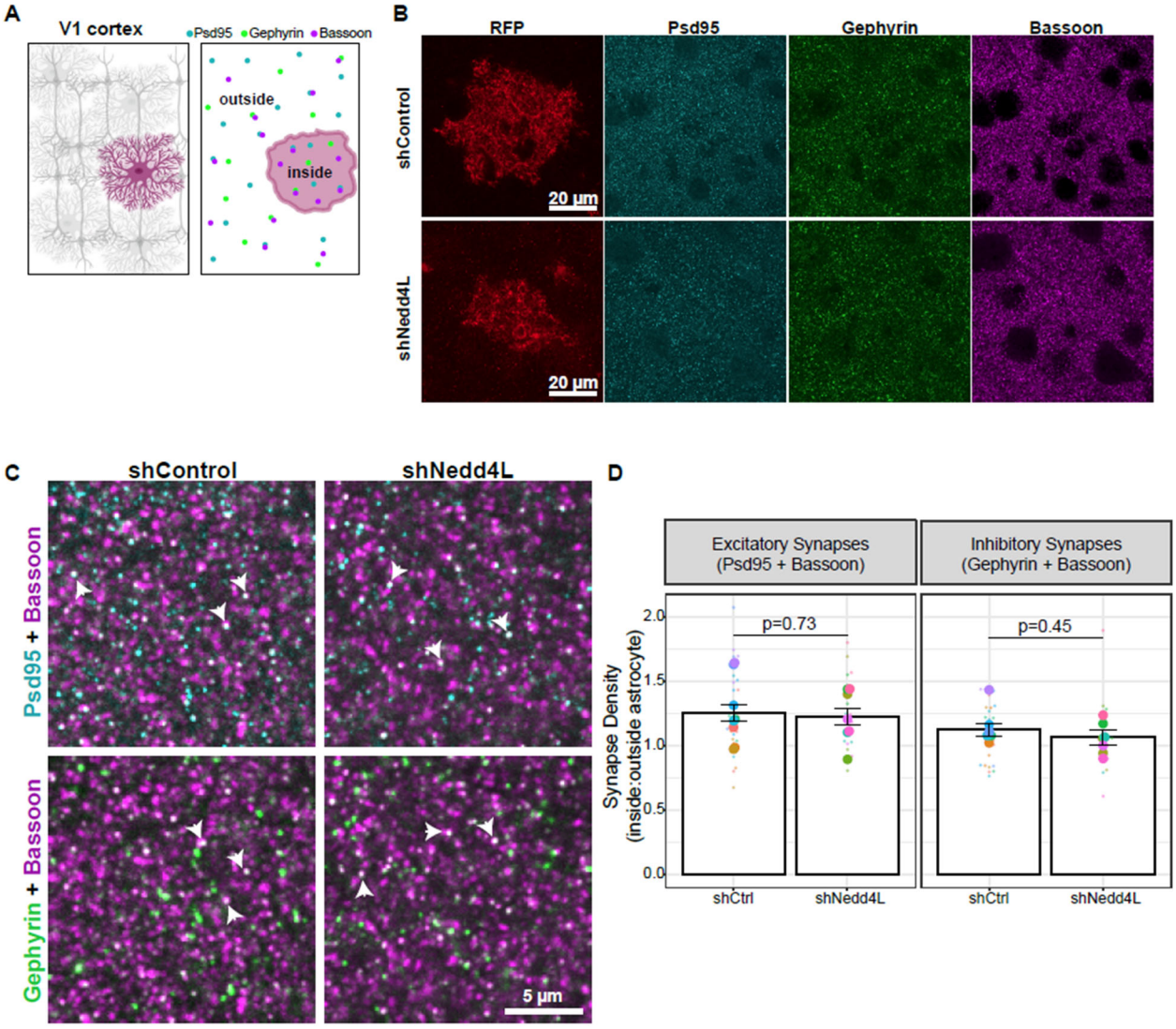

1573

1574 A) Cartoon of analysis. Sparsely labeled astrocytes (shControl mCherry CAAX;
1575 shNedd4l mCherry CAAX) were imaged in P21 mouse V1 cortex. Synapses
1576 (colocalized Psd95 + Bassoon [excitatory synapses] or Gephyrin + Bassoon [inhibitory
1577 synapses]) were quantified within the astrocyte territory (inside) and outside of the
1578 astrocyte territory (outside).

1579 B) Representative images of mCherry-labeled astrocytes (RFP antibody), with Psd95
1580 (cyan), Gephyrin (green), Bassoon (magenta) staining.

1581 C) Magnified image showing colocalized synapse puncta for excitatory (Psd95 +
1582 Bassoon), and inhibitory (Gephyrin and Bassoon) synapses. Colocalized puncta are
1583 shown in white, with examples indicated with arrows.

1584 D) Quantification of synapse density within labeled astrocyte to the outside unlabeled
1585 astrocyte territory. Large dots represent individual animals, with small dots representing
1586 each image from an animal. P-values indicate main effect of linear mixed effects
1587 ANOVA. Excitatory synapses: $F(1,13) = 0.12$, $p=0.73$. Inhibitory synapses: $F(1,13) =$
1588 0.61, $p=0.45$. 7-8 animals were used per condition, with 4-8 images taken per animal.

1589

1590 **Supplemental Figure 7:**

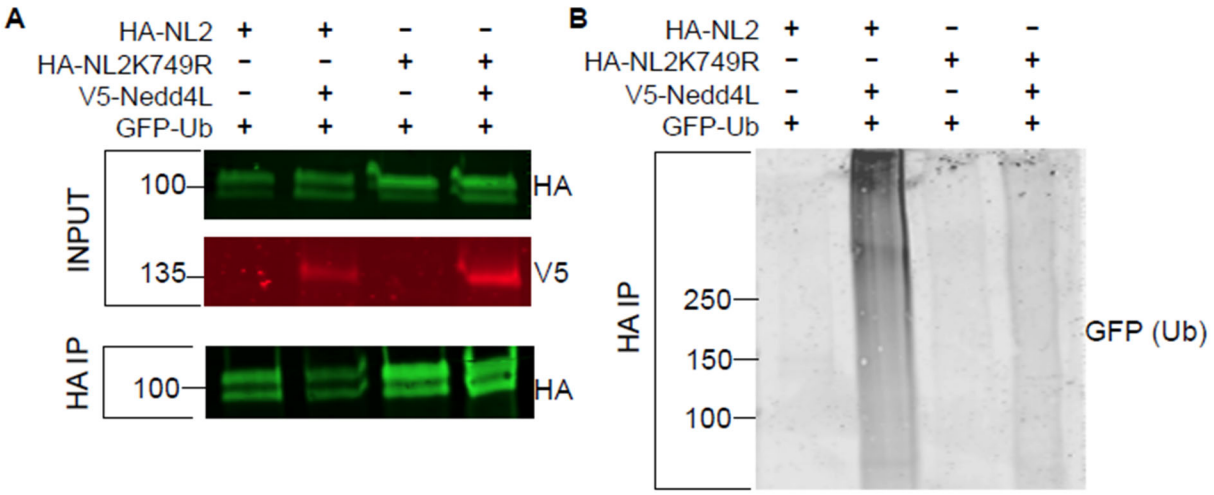

1591

1592 A, B) Western blot from HEK cell lysates and HA-NL2 IPs shows NL2 ubiquitination with
1593 Nedd4l overexpression, which is lost when NL2 is mutated at K749. GFP-tagged
1594 ubiquitin was overexpressed in these cells to visualize ubiquitinated NL2 in the
1595 immunoprecipitation.

1596 **Supplemental Dataset 1: In vivo BioID results.** All proteins significantly enriched in
1597 Astrocytic NL1 (sheet 1), Astrocytic NL2 (sheet 2), Astrocytic NL3 (sheet 3), and
1598 Neuronal NL (sheet 4) iBioID compared to Astrocytic TurboID alone.

1599 **Supplemental Dataset 2: iBioID Gene Ontology output.** All biological process gene
1600 ontology results. Column 1 indicates the iBioID list to which the categories correspond
1601 to.

1602 **Supplemental Table 1: Detailed statistical analyses for each figure panel.**